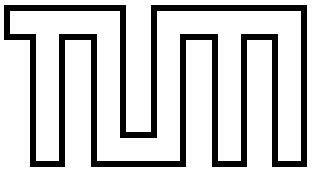

FAKULTÄT FÜR INFORMATIK

DER TECHNISCHEN UNIVERSITÄT MÜNCHEN

Master's Thesis in Biomedical Computing

Efficient and Robust Patient-Specific Model of the Heart Function based on MRI Images

Oliver Zettinig

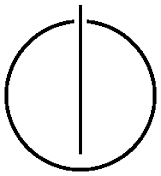

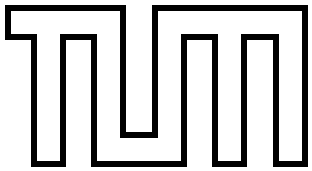

FAKULTÄT FÜR INFORMATIK

DER TECHNISCHEN UNIVERSITÄT MÜNCHEN

Master's Thesis in Biomedical Computing

Efficient and Robust Patient-Specific Model of the Heart Function based on MRI Images

Effiziente und robuste patientenspezifische Modellierung der Herzfunktion basierend auf MRI-Bildern

Author:	Oliver Zettinig
Supervisor:	Prof. Dr. Nassir Navab
Advisor:	Tommaso Mansi, Ph.D.
	Bernhard Fuerst, M.Sc.
Date:	October 15, 2013

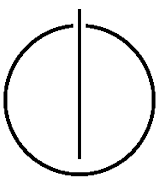

Ich versichere, dass ich diese Masterarbeit selbständig verfasst und nur die angegebenen Quellen und Hilfsmittel verwendet habe.

I assure the single handed composition of this master's thesis only supported by declared resources.

Garching bei München, 15. Oktober 2013 Oliver Zettinig

Supervisors and Collaborators

Technische Universität München, Germany

Prof. Dr. Nassir Navab	Supervisor
Bernhard Fuerst, M.Sc.	Advisor

Siemens Corporation, Corporate Technology, New Jersey, United States

Tommaso Mansi, Ph.D.	Advisor
Ali Kamen, Ph.D.	Advisor
Bogdan Georgescu, Ph.D.	Collaborator
Saikiran Rapaka, Ph.D.	Collaborator
Dorin Comaniciu, Ph.D.	Collaborator

University Hospital Heidelberg, Department of Internal Medicine III, Heidelberg, Germany

Dr. Jan Haas	Clinical Collaborator
Karen S. Frese	Clinical Collaborator
Dr. Farbod Sedaghat-Hamedani	Clinical Collaborator
Dr. Elham Kayvanpour	Clinical Collaborator
Ali Amr	Clinical Collaborator
Prof. Dr. Stefan Hardt	Clinical Collaborator
Dr. Derliz Mereles	Clinical Collaborator
Prof. Dr. Henning Steen	Clinical Collaborator
Prof. Dr. Hugo A. Katus	Clinical Collaborator
Dr. Benjamin Meder	Clinical Collaborator

Siemens AG, Healthcare Strategy, Erlangen, Germany;
Department of Human Genetics, Saarland University, Germany

Dr. Andreas Keller	Collaborator

Acknowledgments

My supervisor, my advisors, and many colleagues and friends have supported me during my studies and in particular throughout the course of this Master's thesis. At this point, I want to thank everyone who helped me toward this great achievement.

The research of this thesis has been performed at Siemens Corporation, Corporate Technology. I am deeply and wholeheartedly grateful to my advisor Tommaso Mansi for his excellent guidance and encouraging supervision. Always believing in me, he has regularly challenged me to exceed my own limitations. During my stay at Siemens, I have learned a lot, ranging from scientific methodology and academic correctness to meticulous writing skills and farsighted vision. I could not appreciate his demanding but very rewarding support more, and my stay in Princeton would not have been the same without him.

Likewise, I want to thank the other members of the team who I had the great opportunity to work with: co-advisor Ali Kamen, Bogdan Georgescu, Saikiran Rapaka, Viorel Mihalef, and Puneet Sharma. I enjoyed working in this inspiring group very much and not only appreciated highly interesting discussions and valuable insight but also the amicable atmosphere. I am especially grateful to Dorin Comaniciu, who granted me the unique experience to present my work at the MICCAI 2013 conference in Japan.

It is my wish to warmly thank my supervisor at Technische Universität München, Nassir Navab, who always found some of his precious time when support was needed most. I appreciated his encouragement while granting me the space to work in my own way.

I am also extremely thankful to my advisor Bernhard Fuerst for his enduring support regarding my thesis and beyond. For many years, his constructive and very useful feedback has served as perfect and reliable orientation. Following his own path first to TUM and later to Siemens, I have always been able to rely on his sincere judgement. Moreover, I am very grateful for his strong motivation, for his remarkable availability and for his help in times of doubt.

I want to thank all my colleagues at Siemens and the chair, who have accompanied me for the last months, especially Richard Brosig for generously spending many hours on expanding my mathematical background, Christian Schulte zu Berge for his smart and pragmatic comments and his expedient feedback, and Angelo Scorza (and his extensively used pocket whiteboard) for eye-opening discussions about algorithmic efficiency.

Finally, I would like to express my gratitude to my family (my parents Gabriela and Raimund, and my sister Désirée) as well as my closest friends, colleagues at university and companions, both at home in Europe and overseas. I am thankful for their great support and perpetual confidence – without them I would not be who I am today.

Thank you!

Abstract

Characterized by a significant enlargement and weakening of the heart, dilated cardiomyopathy (DCM) causes almost a third of heart failures in the Western countries. Since treatment of DCM is complex due to a large variability of etiologies, clinicians require fast and predictive, and therefore personalized computational tools to investigate and better understand pathologies, plan respective therapies and predict their outcomes. However, most recent modeling frameworks are either incomplete in their modeling capacity or unsatisfactory for clinical routine in terms of their computational performance.

In this thesis, fast and robust patient-specific parameter estimation for a biomechanic model of the human heart from clinical and imaging data is investigated. To that end, this work is based on available models of heart anatomy and electrophysiology and firstly presents an integrated framework to compute cardiac motion using a finite element setup. In particular, an efficient strategy to parallelize the evaluation of stress and mechanical boundary conditions was developed, allowing a high-performance implementation of the Holzapfel-Ogden myocardium tissue model and more accurate cardiac motion during isovolumetric phases.

Secondly, this thesis introduces a novel, data-driven approach to calibrate electrophysiology (EP) parameters from clinically available 12-lead electrocardiograms (ECGs). Coupling an existing GPU implementation of a mono-domain Lattice-Boltzmann model of cardiac EP with a boundary element formulation of body surface potentials, we were able to train a polynomial regression model on QRS duration and electrical axis of ECG simulations and predict myocardium diffusion parameters. For the first time, this approach also provides uncertainty estimates of the underlying data.

Using the proposed parallelization strategy, biomechanic model evaluation could be accelerated on average by one order of magnitude. The ECG-based calibration of electrophysiology models has been shown to significantly improve model accuracy compared to nominal diffusivity and to outperform standard optimization techniques in terms of the predictive power. Altogether, the presented framework may help clinicians to offer more personalized treatment and eventually improve the outcome of medical interventions in the future.

Contents

1 Introduction

This thesis deals with the patient-specific parameter estimation of an electromechanic model of the human heart from clinical and imaging data. The research has been performed in the course of an internship at Siemens Corporation, Corporate Technology, Imaging and Computer Vision, Princeton, NJ, USA, and in close collaboration with the chair for Computer Aided Medical Procedures, Technische Universität München, Germany.

This work first gives an overview to the topic and introduces the reader to the medical background in chapter 1, before outlining the state of the art in chapter 2. The methodology of this thesis is presented in chapter 3, and conducted experiments and their results are illustrated in chapter 4 and discussed in chapter 5. The final chapter (6) concludes the thesis and gives an outlook to future challenges.

1.1 Motivation

Dilated Cardiomyopathy (DCM) is defined as a disease of the myocardium in which the heart becomes weakened and enlarged [30]. As a result, the heart is not able to pump sufficient amounts of blood to the rest of the body, affecting organ systems such as the lungs and the liver. The disease is known to be one of the most common causes of heart failure and the leading indication of heart transplantation in younger adults [54].

Diagnosis and treatment turn out to be challenging due to a huge variety of individual causes and disease stages, including previous infarction and various toxic, metabolic or infectious agents. Therefore, clinicians require computational tools to investigate and better understand pathologies, plan respective therapies such as the implantation of artificial pacemakers or cardioverter-defibrillators, and predict their outcomes. In particular, a high rate of non-responders [54] creates a clinical need to determine which therapy may be beneficial for a given patient, and which prerequisites may trigger a successful outcome.

Most recent modeling frameworks suffer from either of the following, opposing limitations: On the one hand, many frameworks offering adequate computational performance are incomplete and hence not precise enough to describe patient-specific characteristics of the disease with satisfactory detail. As the underlying cause of DCM often lies in the dark, it is crucial to capture a broad range of biological phenomena with a sufficient level of detail. On the other hand, fulfilling high modelling requirements often leads to an enormous demand of computational resources. However, stressful clinical workflows and the need for interactive tools for therapy planning form an upper bound in computational power for clinical applicability.

1.2 Problem Statement

To introduce patient-specific prediction of cardiac physiology into the clinical routine, an integrated framework comprised by models of heart anatomy, electrophysiology and biomechanics is required. For accurate physiological predictions of both heart electrophysiology and mechanics, a personalization technique is needed. This thesis addresses the integration of the models, presents a novel strategy for high-performance mechanical stress evaluation, and introduces an estimation of patient-specific electrophysiological parameters to drive the biomechanical model.

In particular, this work presents an integrated framework to estimate cardiac mechanics, including strain and stress throughout the heart cycle. Based on an anatomical model that incorporates a rule-based fiber and fiber sheet architecture, an electrophysiology model is solved on static, end-diastolic geometry. The hereby computed myocyte activation times finally trigger muscle contraction in a finite element-based biomechanical model.

To enable the personalization of biomechanical model parameters, it is necessary to evaluate the finite element framework frequently. Hence, the total computation time for a full heart cycle should be as low as possible, allowing many iterations for sufficient personalization. We therefore propose an efficient strategy to parallelize the evaluation of stress and mechanical boundary conditions, leading to a high-performance implementation of the myocardium tissue model and more accurate cardiac motion during isovolumetric phases. As such, the computation of one complete heart cycle can be achieved fast enough to perform biomechanical model parameter optimization.

Regarding electrophysiology parameter estimation, a novel data-driven approach to calibrate parameters from clinically available 12-lead electrocardiograms (ECGs) is proposed. In this work, an existing GPU implementation of a mono-domain Lattice-Boltzmann model of cardiac EP is coupled with a boundary element formulation of body surface potentials. Thereafter, a polynomial regression model is trained on features of simulated ECG signals to predict myocardium diffusion parameters.

1.3 Medical Background

1.3.1 Cardiovascular System

The human cardiovascular system is the key life-sustaining organ system of the human body. Its purpose is to supply cells throughout the body with oxygen and vital nutrients and provide a means of waste product disposal. Breakdown of the cardiovascular system, such as heart failure or rupture of main vessels, is a dangerous life-threatening condition, which raises a great importance of medical diagnosis and treatment.

Characterized as a closed double-loop, the circulatory system is divided into two main parts: the *pulmonary circulation* and the *systemic circulation*, as illustrated in fig. 1.1. Starting in the right ventricle of the heart (1), oxygen-depleted blood enters the pulmonary circulation via the pulmonary arteries (2) and is pumped into the lungs (3). After oxygenation, the blood returns through the pulmonary veins (4) back to the heart, specifically into the left atrium (4) and the left ventricle (5). There it enters the systemic circulation and is ejected into the aorta (6), which forks into various arteries. In small capillaries in all parts of the body the blood is eventually deoxygenated (7, 8). Finally, the venous system returns

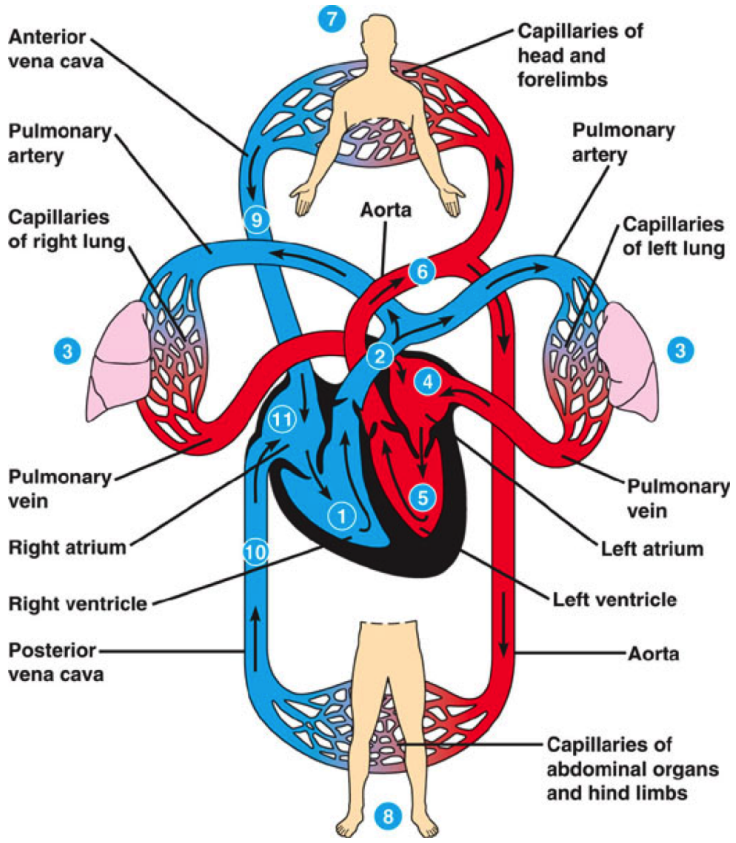

Figure 1.1: Schematic illustration of the cardiovascular system (see text for details). Image from *Anatomisty.com*[1].

the blood via the venae cavae (9, 10) back to the heart, this time into the right atrium (11) and the right ventricle (1) [77].

1.3.2 Heart Anatomy

The heart is an organ of remarkable sophistication and a powerful muscle designed to perpetually transport blood through the cardiovascular system. Evolution has optimized its shape and function toward maximum pump effectivity and minimum muscular work. The heart muscle itself, called *myocardium*, consists of striated muscle tissue and is protected by thin endothelial layers on both sides: the *endocardium* inside the atria and ventricles, and the *epicardium* outside. The heart is isolated from other organs by the *pericardium*, a non-contracting fibrous sac. A thin liquid layer between pericardium and epicardium ensures smooth and almost frictionless cardiac motion [77].

As illustrated in fig. 1.2, the interior of the heart is divided into a left and a right part. These parts correspond to the two sections of the cardiovascular system: the right ventri-

[1] Anatomisty.com. Cardiovascular System. `http://anatomisty.com/anatomy-sistems/cardiovascular-system-2`, accessed on July 14, 2013

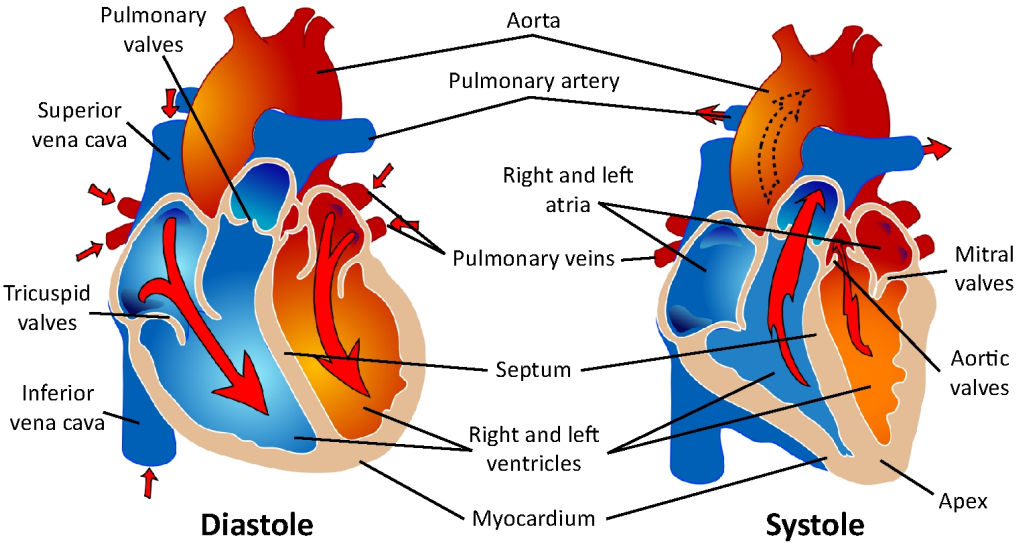

Figure 1.2: Structure of the normal heart. Image from [47].

cle pumps blood into the pulmonary circulation loop, the left ventricle into the systemic circulation loop. Left and right cavities are separated by the *septum*, which belongs to the left heart.

Each side consists of two chambers and two one-way valves out of connective tissue that control the direction of blood flow during the cardiac cycle. Blood enters the heart through veins (vena cava, pulmonary veins) and arrives in the *atria*. The atrioventricular valves, namely the *tricuspid* valve for the right heart and the *mitral* valve for the left heart, ensure blow flow from the atria to the ventricles and not conversely. When the pressure in the ventricles exceeds the pressure in the atria, the valves shut and remain closed. Papillary muscles and the *chordae tendineae* ensure correct valve function and prevent a valve prolapse. The semilunar valves in the arteries leaving the heart, namely the *aortic* and the *pulmonary* valves, similarly ensure unidirectional blood flow and open as soon as the pressure in the ventricles matches the pressure in the arteries. So-called *regurgitations*, backward blood flow due to imperfectly sealed valves, can lead to severe cardiac functional impairment.

Depending on the required muscle workload, myocardium thickness varies over the heart. Since the atria do not need to contract significantly, atrial walls are relatively thin ($\approx 2mm$). The free wall (i.e. the outside myocardium wall) of the right ventricle is slightly thicker ($\approx 5mm$) because the right ventricle is responsible for pumping the blood through the lungs. It is not surprising that the myocardium is thickest in the left ventricle ($\approx 15mm$) due to the great cardiovascular resistance in the systemic circulation. A direct result of this variation in thickness is a significantly different contrast in medical images. While the left ventricle is usually well-defined in MR images, reliable detection of the right ventricle and the atria might be challenging.

1.3.3 Heart Physiology

Cardiac function is automatically and subconsciously controlled by the *autonomous sympathetic system*. Contraction and relaxation of cardiac myocytes are triggered by an electrical wave that propagates over the myocardium. Electrical activation and muscle contraction form a system of tightly coupled and well-balanced biological phenomena. The following sections describe how the electrical wave activates muscle fibers and which molecular systems are responsible for the actual muscle contraction [20].

Electrophysiology

Throughout the myocardium, muscle cells are activated by an electrical stimulus that causes them to depolarize and contract. A coordinated and synchronous global heart contraction requires precise timing of all involved muscle cells for most efficient pumping, which is why the heart possesses a complicated electrical conduction system as shown in fig. 1.3.

The electrical wave is originated at the *sinus node*, often also called sinoatrial node due to its anatomical location. The sinus node serves as physiological pacemaker. Internodal pathways pass through atrial tissue, which cause atrial myocytes to be depolarized, consequently pumping blood into the ventricles. The electrical impulse is purposely delayed at the *atrioventricular* (A-V) node for a couple of milliseconds, which allows the atria to fully contract and pump as much blood into the ventricles as possible. Eventually, the electrical wave is conducted downward toward the tip of the heart (*apex*) through the *bundle branches* at very high speed ($\approx 2000 mm/s$). The *Purkinje fiber* system finally distributes the electrical impulse throughout the remaining myocardium, from endocardium to epicardium, at a much lower speed ($\approx 500 mm/s$) and causes ventricular myocytes to be depolarized and contract.

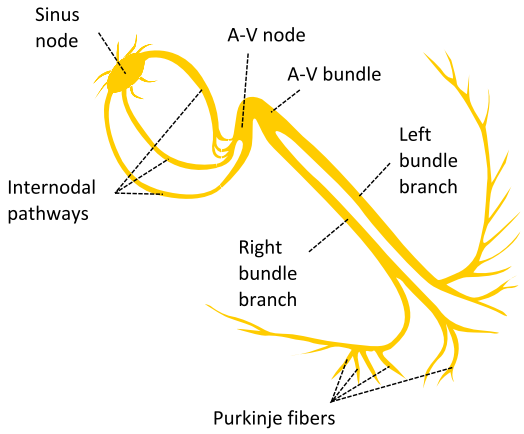

Figure 1.3: Electrical conduction system of the heart. Image from *Wikipedia*[2].

[2]Wikipedia. Electrical conduction system of the heart. http://en.wikipedia.org/wiki/File:Electrical_conduction_system_of_the_heart.svg, May 28, 2009

The propagation of the electrical wave as well as the triggering of muscle contraction is governed by molecular mechanisms based on sodium (Na^+), potassium (K^+), and calcium (Ca^{2+}) ion concentration differences on both sides of the cell membrane. As in other (skeletal) muscles, Na^+ ions flood into the cell through specific ion channels when the cardiac myocyte is stimulated. The cell addresses the significantly increased transmembrane voltage by releasing K^+ ions. However, voltage-gated calcium channels on the cell membrane cause an influx of Ca^{2+} ions at the same time, which induces the release of calcium from the *sarcoplasmic reticulum*, a muscle cell organelle responsible for storing and providing Ca^{2+} ions upon excitation. This so-called *calcium-induced calcium release* (CICR) phenomenon triggers muscle contraction. The temporary depolarization of the cell is referred to as *action potential*. During a short timespan called *refractory period* the cell cannot be excited again and stays contracted. Afterwards, ion concentrations are re-balanced to their initial state and the muscle returns to relaxation. The duration of the action potential (APD) is not constant over the myocardium, and its variation has an influence on the synchrony of the cardiac motion [20].

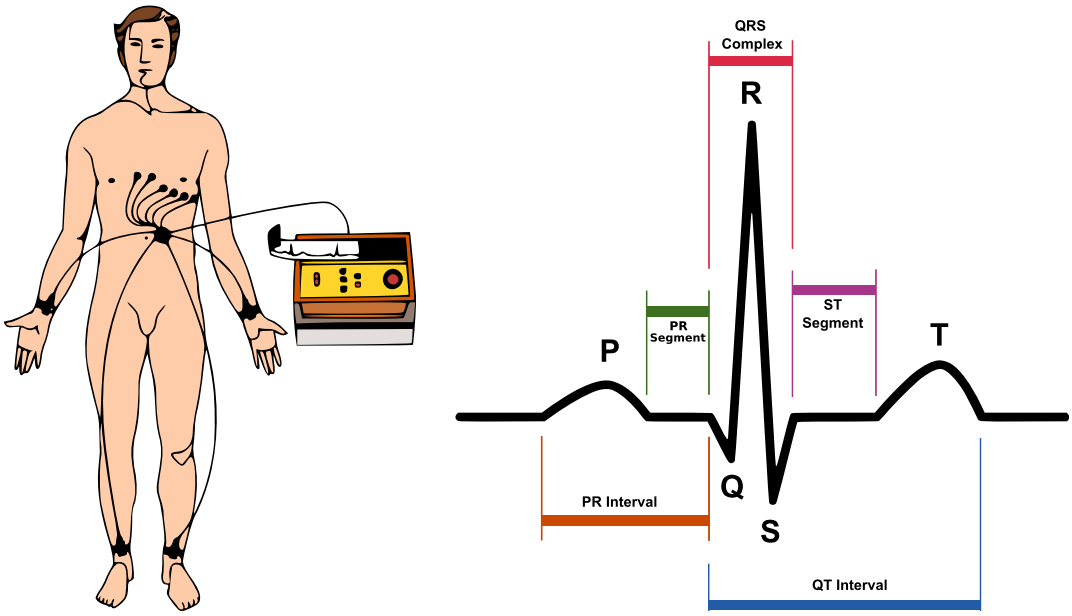

Figure 1.4: **Left:** Patient connected to the 10 electrodes necessary for a 12-lead ECG. **Right:** Representation of normal ECG (lead II). Images from *Wikipedia*[3].

For more than a century, electrocardiography has been utilized to non-invasively analyze cardiac electrophysiology. Today, electrocardiograms (ECG) are an important diagnostic tool in clinical routine. As illustrated in fig. 1.4 (left panel), 10 electrodes placed on patient torso and extremities are necessary for the commonly used 12-lead ECG. Although ECG measurements are summation signals integrating the action potentials of all myocytes throughout the myocardium, the combination of the various leads provides a spatial perspective and allows a quite detailed diagnosis such as the detection of bun-

[3]Wikipedia. Electrocardiography.
`http://en.wikipedia.org/wiki/Electrocardiography`, August 2, 2013

dle branch blocks or severe arrhythmia. Nevertheless, local variations and impairments of cardiac conductivity require different approaches, e.g. invasive endocardial mappings obtained through catheter.

Figure 1.4 (right panel) schematically shows the well-defined ECG signal of healthy subjects. The following patterns, which correspond to specific cardiac events, can regularly be observed [20].

- **P wave**: Initial atrial depolarization triggered by the sinus node
- **PR segment**: Conduction delay at the atrioventricular nodes
- **QRS complex**: Rapid depolarization of right and left ventricles
- **ST segment**: Isoelectric phase during which ventricles remain depolarized
- **T wave**: Repolarization of the ventricles

The leads of a standard 12-lead ECG can be divided into bipolar limb leads, augmented limb leads and precordial leads, only the first of which being bipolar. Fig. 1.5 shows an ECG scan printed on graph reference paper with a common scaling ($1mV$ is represented as $1cm$ on the ordinate, and $1s$ as $25mm$ on the abscissa). The characteristics of the different leads are as follows.

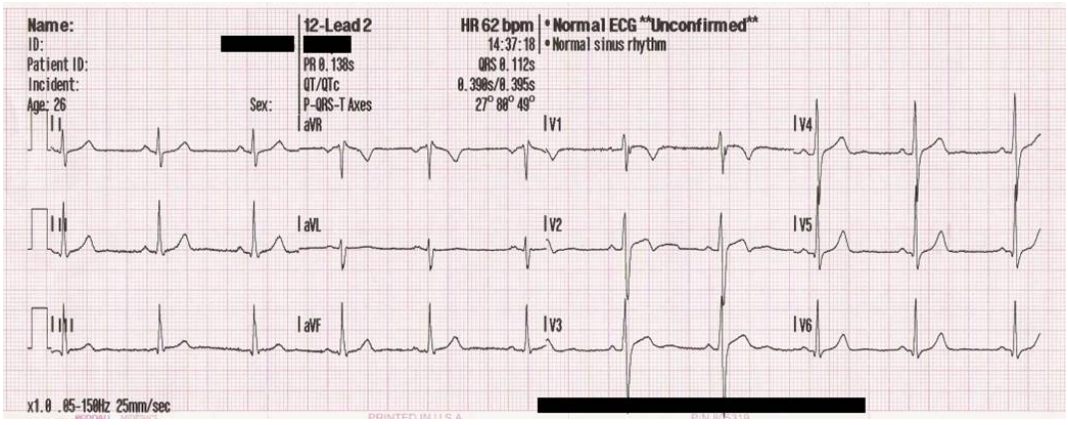

Figure 1.5: 12-lead ECG of a patient with normal sinus rhythm. Image from *Wikipedia*[4].

- **Bipolar limb leads** I, II, III: The three basic leads are computed from the extremity electrodes on left arm (LA), right arm (RA), and left leg (LL):
  $I = LA - RA$
  $II = LL - RA$
  $III = LL - LA$
  After ECG pioneer Willem Einthoven, these leads are also called *Einthoven leads*.

[4]Wikipedia. 12-lead ECG.
`http://en.wikipedia.org/wiki/File:12leadECG.jpg`, November 24, 2008

- **Augmented limb leads** aVR, aVL, aVG: The augmented leads are derived from the same electrodes as the Einthoven leads but allow a view at the heart from different angles:
  $aVR = RA - \frac{1}{2}(LA + LL)$
  $aVL = LA - \frac{1}{2}(RA + LL)$
  $aVF = LL - \frac{1}{2}(RA + LA)$
  Since the negative pole is constructed using a combination of other electrodes, the augmented leads are considered unipolar. After their inventor Emanuel Goldberger, these leads are also called *Goldberger leads*.

- **Precordial leads** V_1-V_6: Finally, the remaining leads are computed by directly relating the six chest electrodes with Wilson's central terminal: $V_W = \frac{1}{3}(RA + LA + LL)$
  Therefore, the precordial leads are also unipolar leads. After their inventor Frank Norman Wilson, these leads are also called *Wilson leads*.

Together with the actual ECG signals, modern detectors automatically perform signal processing and calculate several parameters. Especially important are the *heart rate* (in the example of fig. 1.5: $62bpm$), the *duration of the QRS complex* ($112ms$) and the *electrical axis* during the QRS complex ($88°$). The heart beat needs to be taken into account when assessing the T wave, because, contrary to the QRS complex, the T wave becomes shorter as the heart beat increases. While the QRS duration can provide a hint on the overall electrical conduction velocity in the ventricles, the electrical axis allows an estimation of the average direction of wave propagation. While the electrical axis can be computed for other parts of the ECG signal as well, the term *electrical axis* denotes the axis during the QRS complex throughout this thesis. QRS durations between 60 and $100ms$ are considered normal, higher values may indicate bundle branch blocks. For the electrical axis, angles between $-30°$ and $90°$ are normal, angles below $-30°$ indicate a left axis deviation, angles above $90°$ a right axis deviation.

Since the propagation of the electrical wave controls cardiac contraction, efficient cardiac function is crucially dependent on globally balanced electrophysiology. Local alterations such as reduced electrical conductivity, for instance after a myocardial infarct, can endanger cardiac synchrony. Many sudden deaths are due to local impairments of cardiac electrophysiology [2].

Biomechanics

Cardiac (and skeletal) myocytes, also known as muscle fibers, are of tubular shape, and each contain chains of myofibrils. The rod-like muscle units are themselves organized as a chain of sarcomeres, each delimited by two so-called Z-discs. Between the Z-discs, cylindrical bundles of two types of interleaved protein filaments are stacked. Thick filaments of myosin ($15nm$ in diameter) and thin filaments of actin ($7nm$ in diameter) slide into each other and cause muscle fiber contraction [77].

The physiological details of cardiac contraction are described in the sliding filament model, proposed in 1954 [93]. On both sides of a sarcomere, actin filaments are directly connected to the Z-discs as shown in fig. 1.6. In between, myosin filaments are only indirectly connected to the Z-discs by titin, a thin protein. The essential feature of myosin

proteins are the myosin heads, which are tighly connected to the myosin filament, but can also bind to the actin. This way, the myosin acts like an active ratchet and paddles along actin filaments by repeatedly binding, ratcheting and letting go. Triggered by inflow of calcium ions (Ca^{+2}), myosin heads are enabled and shorten the sarcomeres by progressively sliding outward, toward the Z-discs. As a result, the space between Z-discs and myosin filaments (I-band) shortens, and the space between opposing actin filaments (H-zone) disappears. A release of calcium deactivates the myosin heads, causing unbinding from the actin and relaxation to the rest state [47].

Apart from the molecular processes of biomechanics, also the macroscopic arrangement of myocardial fibers within the myocardium has a significant influence on cardiac contraction [86, 95].

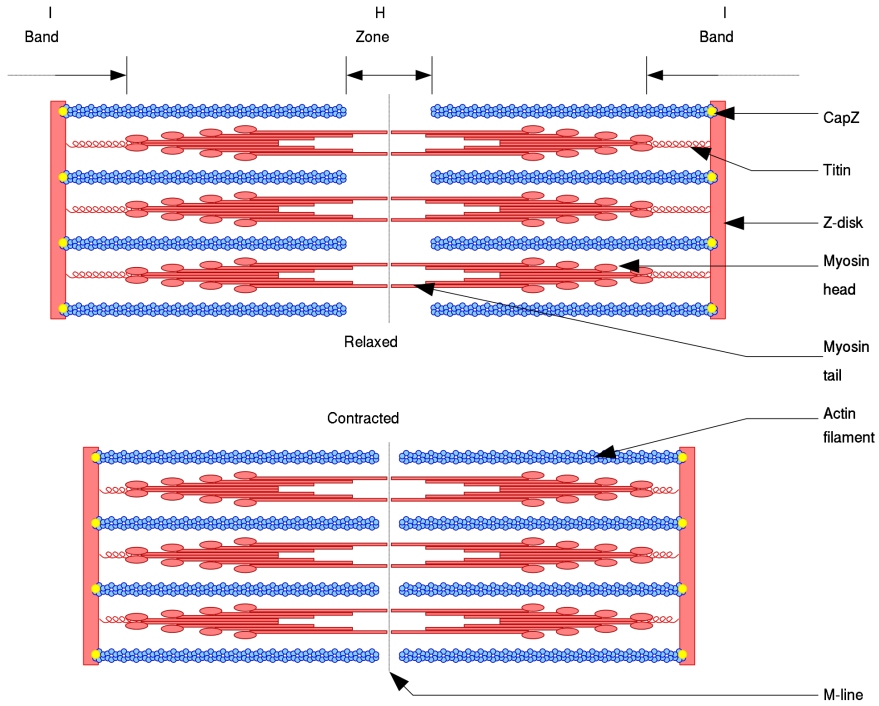

Figure 1.6: Sarcomeres are composed of actin and myosin filaments that slide into each other for muscle contraction. Image from *Wikipedia*[5].

1.3.4 Dilated Cardiomyopathy

Dilated cardiomyopathy (DCM) is a cardiovascular disease in which the heart becomes weakened and enlarged, which leads to an ineffective pump function that can directly and indirectly affect the lungs, liver, and other organ systems [2]. The condition is the most common form of cardiomyopathy. It is known to be one of the most common causes of heart failure and the leading indication of heart transplantation in younger adults [54].

[5]Wikipedia. Sarcomere.
`http://en.wikipedia.org/wiki/File:Sarcomere.svg`, January 10, 2010

Etiology

Very often, no direct cause of DCM is apparent. The disease might be the result of damage to the myocardium due to previous impairment caused by myocardial infarction or due to a variety of toxic, metabolic, or infectious agents. Other possible causes include the abuse of alcohol, pregnancy and chronic uncontrolled tachycardia. Genetic disposition is assumed in approximately 20 per cent [2].

Epidemiology

In the US, the incidence of DCM is 148 cases per 100,000 persons per year, and the estimated prevalence is 920 cases per 100,000 persons. It can occur at any age, including during childhood. The risk of sudden death due to DCM is greatest in patients under 30. Dilated cardiomyopathy occurs more frequently in male patients than in female patients (roughly 3:1) [23].

Diagnosis

The following factors indicate dilated cardiomyopathy:

- General, atrial, ventricular enlargement of the heart
- Sinus tachycardia, atrial fibrillation, ventricular arrhythmias
- Reduced ejection fraction
- Intraventricular conduction defects
- Orthopnea (shortness of breath when lying flat) or cyanosis at rest
- Pleural effusion due to pulmonary venous hypertension

Electrocardiograms are capable of detecting many of the above factors. From an imaging perspective, chest X-rays, and cardiac magnetic resonance imaging (MRI) are predominantly used. To exclude ischemic heart diseases, catheterization examinations and coronary angiography are often employed. As genetic factors for DCM are more and more understood, genetic testing has been utilized to understand the underlying causes of the disease.

Treatment

Since the underlying causes of DCM very often lie in the dark, treatment is based on the relief of symptoms. Standard drug therapies may include salt and alcohol restriction, ACE inhibitors (lowering blood pressure), diuretics (increasing the excretion of water from the body), digitalis (increasing the contraction force) and anticoagulants (preventing clotting of blood).

Depending on the diagnoses impairment of cardiac electrophysiology, patients may receive artificial pacemakers to cope with intraventricular conduction delays. Implantable cardioverter-defibrillators are useful for patients with pronounced risk of arrhythmia. In many cases, heart transplantation remains the ultimate option [2].

1.4 Technical Background

1.4.1 Magnetic Resonance Imaging

Magnetic resonance imaging (MRI) or magnetic resonance tomography (MRT) is a medical imaging technique used in radiology in a wide range of medical applications. In contrast to other imaging modalities such as traditional X-ray, computed tomography (CT), or positron emission tomography (PET), ionizing radiation is not required to visualize internal structures or processes of the body. Offering an excellent image quality both in terms of contrast and resolution, it is commonly used today in clinical routine for diagnostic and also interventional purposes.

MRI is based on the the property of nuclear magnetic resonance of atomic nuclei in the body. This physical phenomenon can be observed when atomic nuclei with an uneven number of spins (e.g. ^1H, ^{13}C) are brought into a static magnetic field. In MRI machines, the nucleus under investigation is ^1H (proton) because biological tissue is mainly composed of water molecules. The static magnetic field will cause the protons' average magnetic moment to be aligned with the direction of the field. Instead of perfect alignment, the individual spins will precess around the field direction with the so-called Larmor frequency. If an external radio frequency (RF) pulse that exactly matches the Larmor frequency is applied, it will be absorbed by the nuclei and their spin will flip. Usually, two different pulses are used: $90°$-pulses will flip the net polarization vector sideways, and $180°$-pulses will flip the orientation completely (from parallel to anti-parallel or the other way round). After the pulse, the spins will relax back to their original configuration, emitting an RF signal termed *free induction decay* in an arbitrary direction that can be measured by receiver coils.

The loss of signal during this relaxation is not desired but can be used to alter the contrast of the image. T_1 relaxation refers to the recovery of longitudinal magnetization and occurs exponentially with a time constant T_1, which is around one second in soft tissue. T_2 relaxation is the loss of phase coherence in the transverse plane and is associated with the number of nuclei in phase. Due to local magnetic inhomogeneities and spin-spin interactions, the relaxation time T_2 is of the order of a few tens of milliseconds in soft tissue. The fact that different tissues have different T_1 and T_2 times is used to create image contrast: By changing the basic parameters of image acquisition *repetition time* (T_R, time between consecutive pulse sequences) and *echo time* (T_E, time between RF pulse excitation and signal reading), T_1-weighted MRI scans (both T_R and T_E short), T_2-weighted MRI scans (both T_R and T_E long) or proton density MRI scans (T_R long, T_E short) can be obtained.

For encoding spatial locations in the patient under examination, three mutually orthogonal gradient fields are used. The first gradient is usually applied in superior-inferior direction and varies the Lamar frequency. As a result, the excitation pulse only causes the spins to flip within a transverse (axial) slice of the body. The second gradient (phase encoding gradient) is applied after the spins are flipped for a short time, resulting in a shift of the spins' phases. Finally, during read-out, the third gradient (frequency encoding gradient) is applied such that the water molecules emit RF signals with spatially varying frequency. The measured signals are line-wise collected in spatial frequency domain termed *k-space*, the 2D Fourier transform of the image to be reconstructed. Inverse 2D Fourier transformation is eventually employed to obtain the actual medical image.

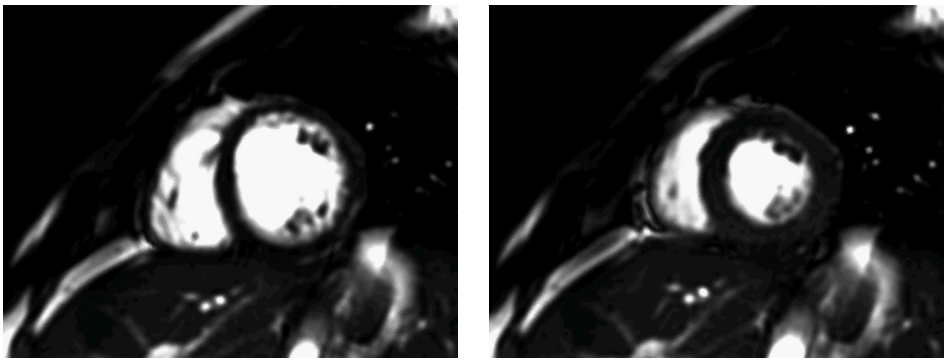

Figure 1.7: Diastolic (left) and systolic (right) short-axis slices of a cine MRI scan obtained from a dilated cardiomyopathy patient.

Cine MRI sequences are 4D scans (3D + time) either acquired in real-time or by using gating. The former technique is only possible with low image quality and temporal resolution. The latter assumes periodicity, acquires data over several periods and reconstructs the final image by splicing data obtained at during different periods but at the same relative time within the period. In cardiac magnetic resonance imaging, ECGs serve as perfect gating signal and allow the acquisition of images with sufficient spatial and temporal resolution. Figure 1.7 shows two slices of a cine MRI sequence obtained from a dilated cardiomyopathy patient.

1.4.2 Finite Element Method

The Finite Element Method (FEM) allows the simulation of various physical phenomena within discretized objects over an also discretized temporal domain. The field of application includes numerical simulations in continuum mechanics, fluid dynamics and thermodynamics. FEM has been established as standard approach for the solution of a wide range of computational problems.

FEM is suited to solve both static and dynamic partial differential equations (PDEs). Using basis functions with finite spatial support, the PDE can be transformed into a system of equations to be solved. In the case of dynamic equations, time integration techniques such as Euler or Runge-Kutta are employed for computation, which are, however, not unique to FEM but can also be applied to alternative methods.

Discretization of Space

Finite elements, from which the name of the method is derived, discretize the spatial domain of the problem. In its simplest form, mesh-based FEM relies on a mesh of triangles (2D) or tetrahedrons (3D), but also other polygonal cells such as hexahedrons (cubes) can be used. However, tetrahedrons are often preferred to hexahedrons because they can more easily be adopted to complicated boundaries and allow a simple generation of volumetric meshes.

Discretization of Time

Mechanical FEM simulation frameworks often solve a second order differential equation of the form:

$$\mathrm{M}\ddot{\mathbf{u}} + \mathrm{C}\dot{\mathbf{u}} + \mathrm{K}\mathbf{u} = \mathbf{F} \tag{1.1}$$

where $\mathbf{u}$ is the vector gathering all mesh vertex displacements. M is the mass matrix, C the damping matrix, and K the stiffness matrix containing the internal elastic forces at each vertex. Finally, the vector $\mathbf{F}$ contains external forces. Summation is used to obtain the global vectors and matrices from the contributions of each element. The dynamics equation can be approximated using an Euler scheme, and the resulting sparse system of linear equations $\Xi\mathbf{u} = \mathbf{F}$ may be solved iteratively using the conjugated gradient algorithm.

1.4.3 General-purpose Computing on Graphics Processing Units

Graphics Processing Units (GPUs) were originally built to allow the fast computation of images in a frame buffer intended for output to a display. Modern computer graphics rendering is very intensive in terms of the number of polygons and pixels to be processed in a short time. Therefore, GPU architectures are designed for a highly parallel execution of code and a high data throughput. As illustrated in fig. 1.8, GPUs contain a multitude of Arithmetic Logic Units (ALU), which can perform computations simultaneously.

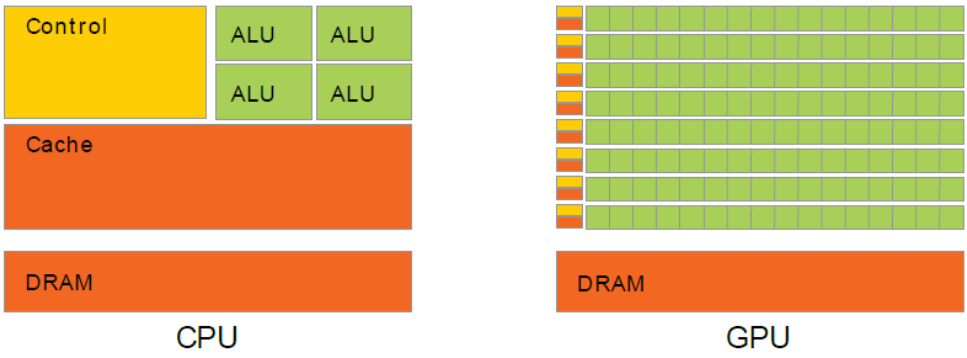

Figure 1.8: Schematic comparison of CPU and GPU architectures. Image from *NVIDIA*[6].

However, the design of GPU architectures only addresses problems that can be expressed as data-parallel computations. Unlike multiple CPU cores, GPU frameworks require the same program to be executed on many datasets. The prohibition of running different code at the same time comes with unique advantages: Because exactly the same hardware-level instructions are executed in all cores (GPU processing elements), sophisticated flow control is as unnecessary as big data caches, because memory access latency can be hidden with arithmetically demanding calculations.

Inspired by the tremendous computational advances of modern GPU cards, the scientific community has discovered the potential of general-purpose computing on graphics hardware in recent years. By exploiting their massively parallel architecture, demanding

[6]NVIDIA Programming Guide for CUDA.
`http://docs.nvidia.com/cuda/cuda-c-programming-guide/index.html`, July 19, 2013

computations can potentially be speed up by several orders of magnitude, depending on the complexity of the algorithm and its implementation.

Nevertheless, a couple of basic principles have to be followed for optimal execution of code on the GPU:

- GPU processing elements, also known as cores or stream processors, are organized in groups (multiprocessors). Each core can execute a sequential thread but all cores of a particular multiprocessor execute in a so-called SIMT (Single Instruction, Multiple Thread) fashion, i.e. that all cores execute the same instruction at the same time. Therefore, forks such as conditional execution branches should be avoided. The two code blocks of an *if* statement, for instance, will be executed sequentially; first the *true* block for all cores in which the *if* condition evaluated *true*, and then the *false* block for the remaining cores.

- As for graphics rendering, single-precision floating point operations were traditionally sufficient, double-precision instructions are either not supported at all or come at the cost of bandwidth. Today, the peak double-precision throughput is usually $^1/_2$ of the single-precision throughput. Hence, calculations should be performed in single-precision, if applicable.

- Regarding memory management, each core has a limited number of very fast registers, and all cores in a multiprocessor share a small software-managed data cache commonly termed shared memory. With a low latency and high bandwidth, this indexable memory runs essentially at register speeds. Shared memory is also the only possibility to allow communication between cores of the same multiprocessor. Parallel implementations often make extensive use of shared memory for optimal execution patterns.

- Without a cache memory hierarchy, instructions in threads issuing a device memory operation may take hundreds of clock cycles due to the long memory latency. Thus, device memory access should be avoided as much as possible. Alignment of memory access (thread 1 reads memory block 1, thread 2 reads memory block 2, etc.) can be resolved faster than random memory access (thread 1 reads block 7, thread 2 reads block 53, etc.) Writing operations to device memory may be cached and are only guaranteed to be reflected until the end of the current program execution. As a result, device memory can not be used as a means of inter-thread communication.

- A program that exploits GPU hardware will regularly 1) copy data from host memory (regular RAM) to device memory (GPU card), 2) execute a function, a so-called kernel, in parallel threads on the GPU, and 3) copy resulting data back from the device to host memory, where it can be further processed.

Vendors of GPU hardware such as NVIDIA or ATI provide computing frameworks to facilitate general purpose GPU programming. In this work, the CUDA (Compute Unified Device Architecture) platform is employed for parallel calculation on graphics hardware. It allows developers to use C/C++ as high-level programming language and offers useful abstractions of hardware specifics as a minimal set of language extensions.

2 State of the Art

The heart is one of the most complex organs of the human body, and its proper functioning is the result of tightly coupled biological systems acting in concert. Due to this outstanding complexity, different aspects of cardiac anatomy and physiology have to be modeled independently. For each aspect, different approaches of varying modeling capacity and computational performance have been proposed. This section gives overview of prior art, focusing on model parametrization and personalization.

2.1 Cardiac Anatomy

Representing the patient-specific anatomy and morphology based on medical images is necessary as a first step toward a complete model of the heart. Apart from the delineation of anatomical structures, it is important to capture the organization of myocytes in fibers and fiber sheets. Since a cardiac anatomy model is usually generated only once for a given patient, computational performance and efficiency is often considered less important than for other components of heart models such as electrophysiology or biomechanics.

2.1.1 Image Segmentation, Detection, Motion Tracking

As outlined in the review of Kang et al. [38], numerous techniques to segment multiple heart chambers from different imaging modalities have been developed. The authors identified four categories of segmentation algorithms: (1) boundary-driven techniques, (2) region-based techniques, (3) graph-based techniques, and (4) model fitting techniques.

The concept of boundary-driven approaches is to deform an initial, estimated contour to the heart boundaries observed in the image. Internal (contour smoothness) and external (image features) energy functionals guide the evolution of the detected boundary in an iterative setup. Popular strategies include active contours [39], commonly referred to as *snakes*, and its more recent adaptations. More recent work includes coupling locally affine registration with an adaption of free-form deformations [102]. The main limitations of theses approaches are the sensitivity to noise and the dependency of the initial contour.

Region-based techniques rely on the partitioning of the entire image domain in regions of interest and background. Clustering [10] and level-set-based approaches [66] may yield global heart segmentation but usually lack chamber-specific detection and are also sensitive to initialization, noise, and image intensity inhomogeneities.

Graph-cut [13] algorithms interpret images as an intensity-weighted graph. Source and sink nodes, which are connected to all image nodes, form a virtual flow through the graph. The optimal segmentation is found as the minimal cost cut separating the image into two different regions. Random walk [28], another graph-based approach, analytically determines the probability that a random walker starting at an unlabeled pixel will first reach

a prelabeled one (seed point). Both techniques, especially the latter one, have successfully been applied to cardiac image segmentation. However, the requirement of seed points may limit full automation.

The last group of algorithms attempts to match a previously defined model of geometric shape to the input image. Implemented as a two-step procedure, the approach first requires a shape model to be constructed from a training set, before matching to a new, unseen image can be performed. Originally expressed as principal component analysis (PCA) on inter-point distance, active shape models (ASM) [17, 57] use key landmark points to generate a statistical description of shape variation. Fitting a model to new points results in minimizing the sum of squared distances between corresponding model and image points in an iterative approach. The biggest advantages of model-fitting strategies are the ability to robustly perform automatic segmentation without manual initialization and the possibility to incorporate very complex geometries such as the human heart with its various chambers, valves and surrounding structures. However, demanding computational performance of the original approach confines modeling capacity.

Recent work has tackled this limitation and developed comprehensive statistical models of the human myocardium. Zheng et al. proposed the marginal space learning (MSL) algorithm for fully automatic segmentation from cardiac computed tomography (CT) [99] or magnetic resonance imaging (MRI) [101] volumes. Instead of exhaustively searching the original parameter space, only low-dimensional marginal spaces are searched, significantly improving detection speed. Refinements to accurately detect left heart valve structures [37] facilitate further automatic processing as physiological landmarks allow semantic associations to the underlying anatomy. Probabilistic boosting trees (PBT) as introduced by [91] have been applied to train discriminative classifiers in datasets with large intra-class variability [79].

Atlas-based segmentation algorithms are related to shape model approaches. An atlas is defined as a segmented reference image constructed from one or multiple (manually) annotated datasets. Using non-linear image registration, the reference segmentations is transferred to the new image [45]. Recent advancements include incorporating multiple atlases of different imaging modalities such as computed tomography angiography (CTA) [42, 103].

Once an end-diastolic image is successfully segmented, continuous detection (ideally with point correspondences) in 3D+time datasets such as cine MRI images is often required. Motion manifold learning [96] is a state-of-the-art method for estimating temporal components. The approach can be used to obtain heart structure segmentation throughout the cardiac cycle.

2.1.2 Cardiac Fiber and Sheet Architecture

Not only for cardiac contraction but also for the propagation of the electrical wave, myocardial fibers play a crucial rule. First, the myocardium tissue has orthotropic mechanical properties defined by the orientation of fibers and their arrangement in fiber sheets. And second, fiber orientation influences the electrical conductivity since the activation wave propagates faster along the fiber direction.

Diffusion tensor imaging (DTI) has been widely used to study the distribution of fiber directions across the myocardium on *ex vivo* human and animal heart preparations [71, 86].

Incorporating fiber architecture into a patient-specific model would ideally rely on *in vivo* measurements, which are not yet clinically available [95]. However, recent progress has lead to *in vivo* acquisitions of fiber orientation with limited resolution, and approaches using an unscented Kalman filter [60] or exploiting properties of Maurer-Cartan connection forms [69] have been proposed to reconstruct fiber orientations from sparse measurements.

One alternative is the creation of fiber orientation atlases from dog [68, 70] or human hearts [44]. While being based on actual measurements, validation studies regarding the compatibility with pathological variations are still pending. The other option are rule-based methods. General patterns of fiber alignment are derived from *ex vivo* studies (as cited above), and translated into a mathematical formulation [7, 58]. Hereby, the fiber elevation and the fiber sheet transverse orientation are fixed on the endocardia and the epicardium and accordingly interpolated throughout the myocardium. The advantage of rule-based approaches over atlases is their parametrization ability, which allows patient-specific adaption to pathologies.

2.2 Cardiac Electrophysiology

Governing muscle contraction, cardiac electrophysiology is an important part of a complete heart model. Being a time-dependent process, electrophysiology needs to be computed over at least one, in many cases multiple full heart cycles. Hence, runtime performance needs to be considered. In addition, model personalization is crucial to obtain patient-specific simulation results.

2.2.1 Model Selection

A plethora of models with different biological scales and theoretical complexity has been proposed since the early works of Hodgkin and Huxley [32] in 1952. Following the classification of Clayton and Panfilov [16], the various models can be divided into three groups: Biophysical, phenomenological and Eikonal models.

Biophysical approaches tackle modeling of cardiac electrophysiology directly at cell level and try to simulate the biological phenomena that are responsible for the myocytic depolarization and repolarization events. In particular, ionic interactions within the cell and across the cell membrane (ion channels) are considered [46, 64, 65]. Since cell functions are complex, more then 50 parameters related to various interactions are required to provide a sufficient degree of detail. The recently proposed model by Ten Tusscher [89] is based on experimental data on most of the major ionic currents and has been shown to reproduce different electrophysiological behaviors such as action potential restitution and conduction velocity. Due to the huge amount of parameters and their often abstract nature (i.e. not mensurable), personalizing biophysical models is challenging.

Embedding the cell model into tissue (and ultimately organ) scale is achieved using semi-linear reaction-diffusion partial differential equations (PDE). Regarding the way the interstitium is modeled, two different strategies have been studied: While mono-domain approaches neglect interstitial effects and consider the myocardiam as single excitable tissue [19], bi-domain approaches superimpose intra- and extra-cellular domains, both of

which existing throughout the entire myocardium, and take different electrical properties into account [12]. The latter kind of models is naturally more computationally demanding than the former approaches but better suited when phenomena between cells and interstitium or entirely within the interstitium are investigated.

Working on a more macroscopic level, phenomenological models are simplifications of biophysical models and were historically the first models to be proposed [24]. They are derived from experimental observations and describe the action potential with a small number of parameters that influence its shape directly, disregarding the underlying ionic interactions. The Mitchell-Schaeffer model [56], for instance, simplifies ion channel interactions to only two currents (an inward and an outward one), and its governing equations only depend on five parameters. As a result, phenomenological models are a reasonable compromise between physical modeling capacity and computational performance when integrated to organ level. In terms of personalization, both the small number of parameters and their direct influence on mensurable output (action potential shape, ECG) facilitates patient-specific simulations.

Similar to biophysical models, phenomenological models are also embedded to organ scale utilizing PDEs in mono-domain [22, 56] or bi-domain [16] frameworks. Recent numerical solutions enable near real-time computation of mono-domain approaches [87]. Especially employing a Lattice-Boltzmann formulation has skyrocketed the computational performance with tremendous speed gains [27, 74].

Eikonal models neglect the simulation of action potentials entirely and reduce muscle activation solely to the propagation of the electrical wave. Therefore, they are a further simplification of the models mentioned above. Mathematically, Eikonal relate a given spatial location in the myocardium with the time of wave arrival [25, 40]. Governed by only one or two parameters, full-heart simulations can be computed very efficiently using fast marching methods [84] and are therefore suited for real-time applications [82]. While it has become possible to simulate wave reentry phenomena with Eikonal models [67], many other pathological conditions such as arrhythmias, fibrillations or tachycardia are believed – in contrast to biophysical or phenomenological models – to be out of reach.

2.2.2 Parameter Personalization

Finding patient-specific electrophysiology parameter combinations is difficult in clinical applications. Current approaches rely on invasive endocardial mapping [75] or body surface mapping (BSM) [21, 92] and employ inverse problem methods to estimate electrical diffusivity or action potential duration. These methods are in general computationally demanding because hundreds of forward model runs are necessary. In addition, the lack of availability of these diagnostic modalities in clinical routine imposes a limitation: Invasive measurements are often avoided, whereas BSM is still not widely available.

2.3 Cardiac Biomechanics

Two different aspects of biomechanics, which are linked together according to the Hill-Maxwell framework [26], have to be considered: The passive constitutive law describes the elastic behavior of the non-linear, anisotropic visco-elastic myocardium tissue and the resulting internal forces. The active component models the muscle contraction controlled by electrophysiology and is usually incorporated as transient external forces [34]. Similar to electrophysiology, the time-dependent process of cardiac biomechanics raises major challenges regarding computational performance for clinical application.

2.3.1 Passive Myocardium Properties

Covering different degrees of complexity, a large variety of models has been proposed to simulate the passive properties of myocardium tissue. In general, improved model accuracy comes with an increasing number of parameters and elevated computational complexity.

Well suited for real-time applications, mass-spring systems have been applied for biomedical simulations [59]. Since they cannot, however, incorporate physical material properties such as Young modulus or Poisson ration, physically realistic simulations traditionally rely on finite element methods (FEM).

A basic simplification is to assume a linear relationship between strain and stress, leading to transverse isotropic linear elasticity [83]. The law is traditionally implemented within the infinitesimal, linear strain theory for computational efficiency, which becomes inaccurate for large deformations. In addition, usually only anisotropy along the fiber direction is considered, leaving the effect of fiber sheets to be neglected.

Based to mechanical *ex vivo* experiments stretching slabs of myocardium tissue in different directions and measuring tissue strain under known load, several non-linear constitutive laws have been derived. A transverse isotropic strain energy density function called *Guccione* law was proposed in [29]. Today, the most commonly used models are the *Pole-Zero* law [36] and the *Costa* law [18], both of which include the effects of myocardial fiber sheets and thus better capture myocardium thickening during systole. In a quantitative comparison [78], the author discovered that the *Costa* law tended to outperform other models in terms of prediction accuracy with respect to *ex vivo* experiments but could not reach a consensus in the scientific community. Extensively used in mechanical engineering to simulate rubber-like materials, Mooney-Rivlin models have also been adapted to biomedical settings with satisfying results [14, 51]. Finally, the recently proposed *Holzapfel-Ogden* constitutive law [33] is based on considerations of the myocardial tissue structure rather than fitting exponential functions to stress-strain experiential data.

2.3.2 Active Myocyte Contraction

Similar to electrophysiology models, the literature distinguishes three categories of active contraction models: Biophysical, phenomenological and lumped models.

Biophysical models are based on experimental *ex vivo* studies [62, 90] and simulate the molecular processes leading to cardiac motion, including ion interactions and actin-

myosin bindings. The *Hunter* model [35] and its more recent extension [63] are commonly used for organ level simulations and require calcium concentrations to be computed directly by the chosen electrophysiology model. The standard model for single cell simulations is the *Rice* model [76], which captures the majority of the cellular mechanisms involved in myofilament function. The model has two disadvantages: First, it requires more then 40 ordinary differential equations (ODEs) to be integrated in each time step. And second, the huge number of parameters (44) imposes a challenge in personalization from clinical data. Nevertheless, organ level integration might be less computationally demanding than expected because sarcomere force dynamics can surprisingly be described on a linear manifold despite the model's non-linear equations [49].

Phenomenological approaches try to allow multi-scale integration by mathematically bridging the gap between the organ level and biological mechanisms at cell level. By simplifying (sub-)cellular mechanisms, a small set of parameters (usually 4-5) and a well administrable number of equations is imposed. The model proposed in [81], which is based on [8], assumes direct relationship between the action potential and the active contraction with the rates of ATP binding and release. The few clinically-related parameters and its computational efficiency encourage clinical application, and preliminary validation studies reported promising predictions [80].

Capturing the essential molecular pathways, the multi-scale model recently proposed in [14], an extension of [8], takes energy exchange during the heart beat into account, linking blood flow and myocardium biomechanics. It showed superior results in [80] and can be used without calcium concentrations being computed by the electrophysiology model.

Neglecting spatial variability, lumped models as analytical descriptions of fiber contraction do not require meshes to be solved. Instead, they focus on one single myocyte and can be solved very efficiently [4]. However, regional abnormalities of the myocardium such as scars or localized fibrosis cannot be captured.

2.3.3 Efficient FEM Implementation

Originally proposed to improve the accuracy of infinitesimal strain implementations, corotational approaches compute deformations in a local coordinate system that rotates with the elements [61], and have been successfully applied to heart simulations [50]. Alternatively, the formulation of Total Lagrangian Explicit Dynamics (TLED) [55] allows sufficient deformation, is also compatible with non-linear tissue models, but requires tiny time steps for numerical stability, especially for stiff materials. Exploiting the massively parallel architecture of Graphics Processing Units (GPU), non-linear TLED solvers have shown significant speed-ups of up to 17x for surgical simulations [88].

Implicit integration schemes [5] are numerically more stable and generously allow larger time steps. However, total Lagrangian formulations of the method require complex derivative expressions and matrix inversions for each time step. The underlying idea of the Multiplicative Jacobian Energy Decomposition (MJED) algorithm [52] is to decompose the strain energy function in such a way that matrix inversions can be avoided. Forces and stiffness matrices are computed directly by deriving the energy with respect to the nodal position.

3 Methods

3.1 Overview

Figure 3.1 shows the four components of the complete heart model. A patient-specific anatomical model constitutes the modeling basis, is derived from imaging data and incorporates structural information regarding the arrangement of myocytes in muscle fibers and sheets. Cardiac electrophysiology models compute the depolarization and repolarization of muscle cells as the electrical wave propagates through the myocardium. In the biomechanics component, an orthotropic material law models the passive properties of myocardium tissue. An active contraction model integrates muscle forces into the framework by relating electrophysiological activation with a simplified description of actine / myosine interactions. Finally, lumped models of cardiac hemodynamics and other constraints are employed to compute biomechanical boundary conditions.

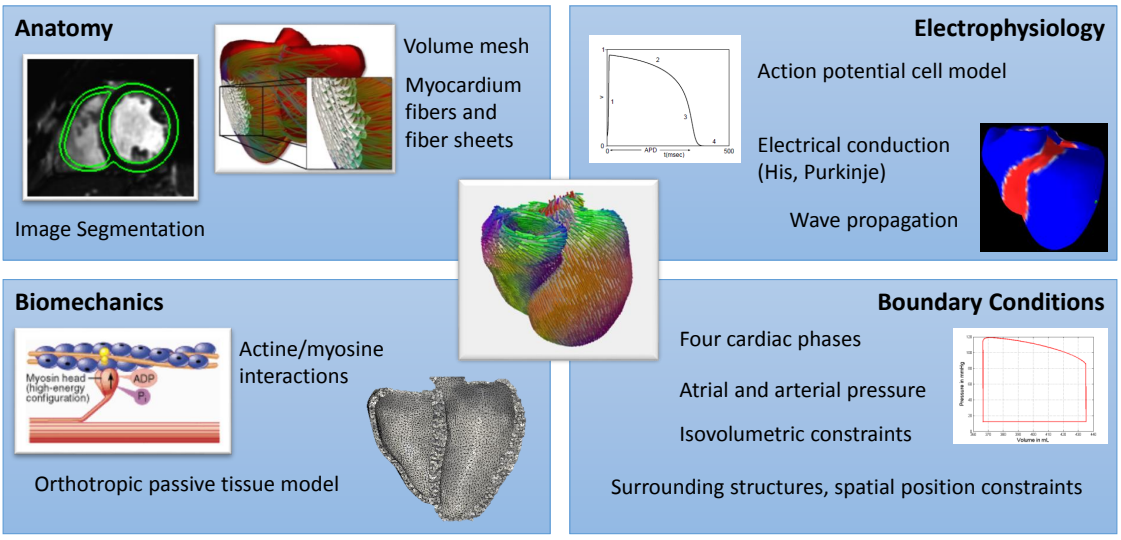

Figure 3.1: Overview of four components of modeling framework. Images partly from [47, 53] modified.

This chapter illustrates the proposed modeling framework in detail and explains how the various components are personalized or calibrated. In section 3.2, the pipeline of anatomical model generation is outlined. The resulting anatomical model is intrinsically personalized since the pipeline is based on medical imaging data. Section 3.3 does not only describe the electrophysiology model employed for heart simulations, but also explains the proposed calibration procedure in detail. Eventually, section 3.4 presents the finite element framework utilized to perform simulations, including active and passive

myocardium stress models and boundary conditions. The section emphasizes on the proposed strategy to efficiently parallelize the evaluation of these models, facilitating the estimation of biomechanical model parameters by significantly reducing the time required for full heart cycle simulations.

3.2 Cardiac Anatomy Modeling Pipeline

Figure 3.2 shows the entire pipeline of cardiac anatomy model generation. Since this work mainly focuses on the electrophysiology and biomechanics parts, the anatomy modeling pipeline is only outlined because providing full insight on the used statistical tools would exceed the scope of this thesis.

First, the patient-specific heart morphology is automatically estimated from magnetic resonance images (MRI) using a database-guided machine-learning framework. A mean-shape model of the heart is registered to the image by automatically detecting its global position, orientation and scale using Probabilistic Boosting Tree and Marginal Space Learning [101]. An active shape model is then applied to refine the borders of the heart in the images [100]. The segmentation process is fully automatic but under expert guidance to allow manual adjustments when necessary.

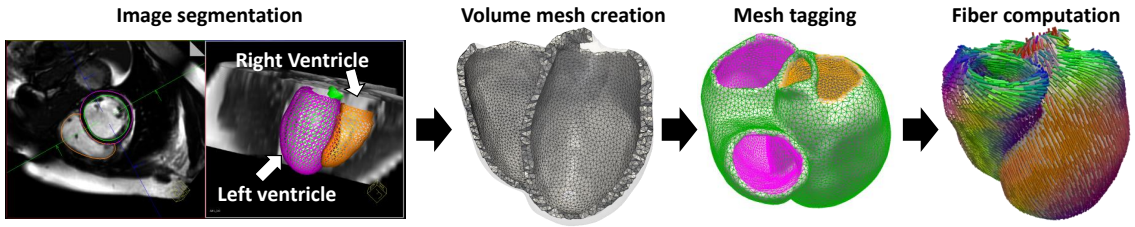

Figure 3.2: Different steps of our automatic pipeline for the estimation of patient-specific anatomical models [98].

The detection algorithm results in three triangulations with point correspondences: *left ventricle endocardium*, *right ventricle endocardium* and *epicardium*, which are then fused to form a closed surface of the biventricular myocardium. Next, a tetrahedral volume is computed using CGAL[1], which is an open-source software library of geometric data structures and algorithms. The facets are tagged with the labels *left ventricle endocardium*, *right ventricle endocardium*, *epicardium*, *left ventricle septum* and *right ventricle septum* automatically according to the point-to-mesh distance between the volume mesh and the detected triangulations.

Finally, a generic model of myocardium fiber architecture that includes fiber and fiber sheets is computed. Unfortunately, diffusion tensor imaging (DTI) is not yet clinically available [95]. Hence, we follow a rule-based strategy [7], which we extend to cover the entire ventricle from apex to valves. As illustrated in fig. 3.3 (A), below the basal plane (identified automatically using the point correspondences of the initial triangulations), the fiber elevation angle α, i.e. their angle with respect to the short axis plane, varies linearly

[1]Computational Geometry Algorithms Library, `http://www.cgal.org`

across the myocardium, from -70° on the epicardium to +70° on the endocardium. Similarly, the sheet direction, which is defined by the angle β with respect to the outward transmural axis, varies transmurally from +45° on the epicardium to -45° on the endocardium. Angles α are computed for each point of the volume mesh between the apex and basal plane based on the geodesic distance to the endocardia and epicardia identified by the facet tags:

$$\alpha = \frac{d_{epi}\,\alpha_{endo} + d_{endo}\,\alpha_{epi}}{d_{endo} + d_{epi}} \tag{3.1}$$

$d_{epi}, d_{endo}, \alpha_{epi}$ and α_{endo} are the distances and angles at the endocardium and epicardium respectively. Angles β are computed in a likewise fashion.

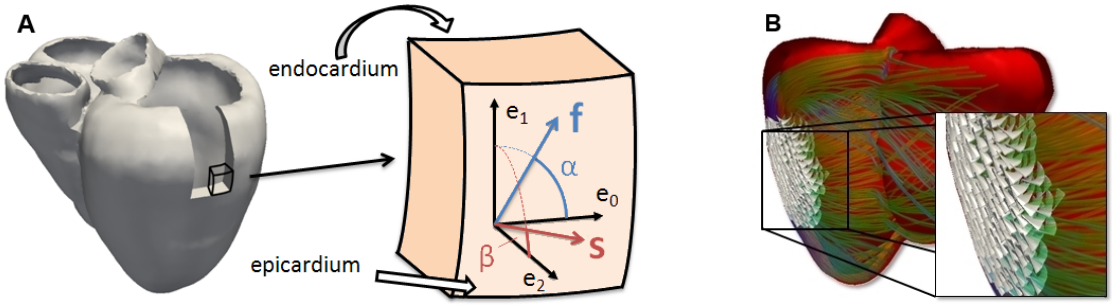

Figure 3.3: **A**: Definition of fiber directions **f** and sheet directions **s** in terms of angles α and β ($\mathbf{e_0}$ circumferential axis, $\mathbf{e_1}$ longitudinal axis, $\mathbf{e_2}$ transmural axis). **B**: Fiber and sheet model computed on a patient-specific anatomy [98].

We then fix the fiber and sheet orientations around each valve (fibers are longitudinal around the aortic valve, tangential elsewhere [58], sheet normals are oriented toward the barycenter of the valves) and interpolate the local orthonormal basis from the basal plane to the valve, first by following the myocardium surface, then throughout the myocardium thickness.

For orthonormality preservation, the interpolation is performed using the Log-Euclidean framework [3]. First, the matrix logarithm of each vertex' fiber and sheet basis B_i is computed, which is trivial since there is no need to diagonalize bases:

$$L_i = B_i W B_i^{\mathsf{T}}, \text{ with the tensor weighting } W = log \begin{pmatrix} 0.9 & 0 & 0 \\ 0 & 0.5 & 0 \\ 0 & 0 & 0.1 \end{pmatrix} \tag{3.2}$$

Second, the barycentric interpolation is performed in log space:

$$L = \frac{1}{4}\sum_i L_i \tag{3.3}$$

At last, the interpolated orthonormal basis is obtained by diagonalization of $exp(L)$ such that the eigenvector of greatest magnitude corresponds to the fiber direction, the eigenvector of second greatest magnitude corresponds to the fiber sheet direction, and the eigenvector with smallest magnitude corresponds to the transversal direction. Figure 3.3 (B) shows the generated fiber and sheet directions.

3.3 Cardiac Electrophysiology

3.3.1 Myocardium Transmembrane Potentials

Cardiac electrophysiology is solved using the Mitchell-Schaeffer model [56], a phenomenological mono-domain model that describes the transmembrane potential $v(t)$ in the interval of $[-70\,mV, 30\,mV]$ throughout the myocardium with the following equation:

$$\frac{\partial v}{\partial t} = J_{in} + J_{out} + J_{stim} + c\nabla \cdot D\nabla v \tag{3.4}$$

Hereby, c is the diffusion coefficient along the myocardial fiber, and $D = \rho \mathrm{I} + (1-\rho)\mathbf{f}\mathbf{f}^\intercal$ the anisotropic diffusion tensor along the fiber direction $\mathbf{f}$ with anisotropy ratio ρ. The model simplifies all ion channel interactions to only two currents. J_{in} denotes an inward gated current, capturing the fast acting ionic currents in the myocyte. The gating variable $h(t)$ models the state of the ion channels and is defined dependent on the change-over voltage v_{gate}. Accounting for transmembrane voltage decrease, J_{out} is an ungated outward current. In addition, J_{stim} refers to a transient stimulus current which is added to mimic electrical pacing. The four parameters $\tau_{in} \ll \tau_{out} \ll \tau_{open}, \tau_{close}$ are directly related to the shape and duration of the action potential, as illustrated in fig. 3.4.

$$J_{in} = \frac{h(t)v^2(1-v)}{\tau_{in}}, \text{ with } \frac{dh}{dt} = \begin{cases} \frac{1-h}{\tau_{open}}, & \text{if } v < v_{gate} \\ \frac{-h}{\tau_{close}}, & \text{otherwise} \end{cases} \tag{3.5}$$

$$J_{out} = \frac{-v}{\tau_{out}} \tag{3.6}$$

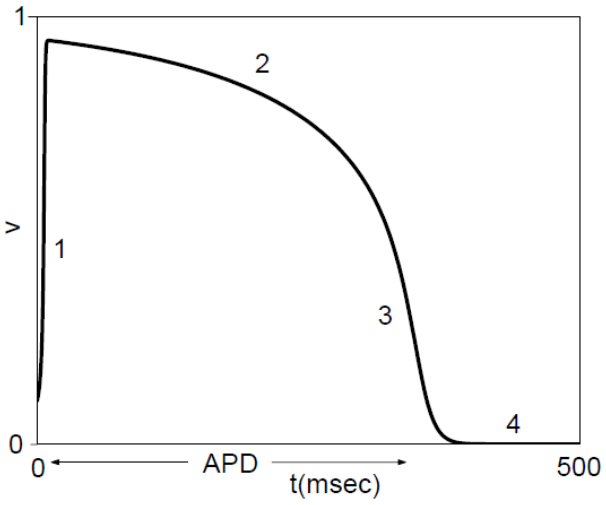

Figure 3.4: Action potential of the Mitchell-Schaeffer model. (1) After the stimulus, the voltage rises quickly with a time constant of τ_{in}. (2) The gate closes, inward and outward currents remain balanced on a time scale of order τ_{close}. (3) The voltage drops as the outward current dominates on a time scale of order τ_{out}. (4) The gate slowly reopens, the recovery constant is τ_{open} [56].

The given partial differential equation (PDE) is solved using the LBM-EP algorithm [74]. LBM is short for *Lattice-Boltzmann method* and was originally developed from cellular automata models of fluid flows. It provides very high scalability on modern computing architectures due to local computations and offers second-order accuracy in space.

The algorithm operates on a Cartesian grid and employs a 7-connectivity topology (6 connections plus the central position) and Neumann boundary conditions. For each of the seven connections $i \in [1, 7]$, the function $f_i(\mathbf{x}, t)$ represents the probability of finding a particle travelling along the respective edge $\mathbf{e}_i$ of node $\mathbf{x}$. Its computation is decomposed into two consecutive steps, namely the *collision* phase, yielding intermediate post-collision states f_i^* and the *streaming* phase, propagating the distribution functions along their corresponding edges:

$$f_i^* = f_i - A_{ij}\,(f_j - \omega_j v) + \delta t\,\omega_i(J_{in} + J_{out} + J_{stim}), \tag{3.7}$$

$$f_i(\mathbf{x} + \mathbf{e}_i, t + \delta t) = f_i^*(\mathbf{x}, t) \tag{3.8}$$

The matrix $\mathrm{A} = (A_{ij})$ denotes the collision matrix that relaxes the distribution function f_i toward the local value of the potential v. The reader is referred to [74] for the derivation of matrix A such that anisotropic fiber-related diffusion is taken into account. The weighting factors ω_i depend on lattice connectivity and emphasize the center position. Since the gating variable $h(t)$ is expressed as ordinary differential equation, it is easily updated at every node using a forward Euler scheme. Finally, the transmembrane potential $v(\mathbf{x}, t)$ is expressed as:

$$v(\mathbf{x}, t) = \sum_i f_i(\mathbf{x}, t) \tag{3.9}$$

Inherently being node-wise, the strictly local collision rule can be implemented very efficiently on a GPU architecture. The anatomical model at end-diastasis is represented as a level set, simplifying the processing of complex geometries including the respective boundary conditions. As shown in fig. 3.5, five domains are considered: Left and right ventricular septum, used to pace the heart to mimic the His bundle; left and right endocardia with fast electrical diffusivity, c_{LV} and c_{RV}, to mimic the Purkinje network, and the remaining myocardium tissue with diffusivity c_{Myo}. The resulting transmembrane potentials are mapped back from the Cartesian domain to the tetrahedral volume mesh using tri-linear interpolation.

Solving cardiac electrophysiology serves two different purposes: On the one hand, the computed transmembrane action potentials are directly used in the biomechanical model to trigger muscle contraction, as described further down in section 3.4. On the other hand, the calculation of the action potential distribution on the heart surface is the first step toward ECG calculation and our data-driven model calibration as explained subsequently.

3.3.2 Boundary Element Model of Torso Potentials

Since the Mitchell-Schaeffer model is a mono-domain model, it only provides transmembrane action potentials. However, for a projection to the torso, extracellular potentials at the epicardium are required. To estimated them, the elliptic formulation proposed in [15] is used, which assumes a constant diffusion anisotropy ratio $\lambda = c_i(\mathbf{x})/c_e(\mathbf{x})$, with c_i and

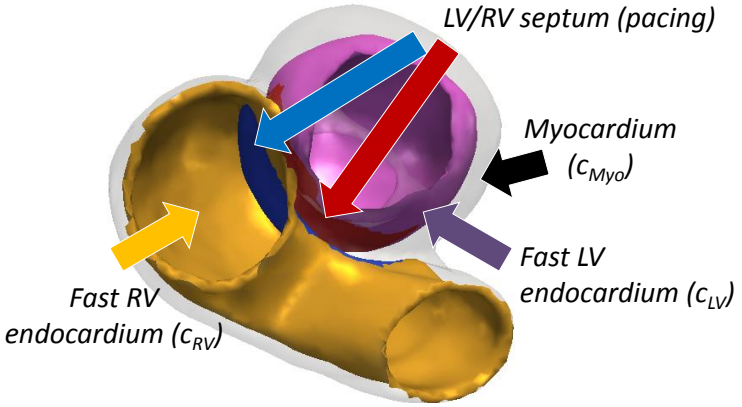

Figure 3.5: Myocardial domains considered in EP simulation [97].

c_e denoting the intra- and extracellular diffusion coefficients respectively. This approach has been shown to preserve the essential ECG features well [11, 15]. Within the entire myocardium domain Ω, the extracellular potential ϕ_e is expressed as:

$$\phi_e(\mathbf{x},t) = \frac{\lambda}{1+\lambda}\,\frac{1}{|\Omega|}\int_{\Omega}(v(\mathbf{y},t)-v(\mathbf{x},t))d\mathbf{y} \tag{3.10}$$

A boundary element method (BEM) [6, 85] is employed to map ϕ_e from the epicardium surface mesh (a subset of the tetrahedral volume mesh) to the torso, which is also discretized as a triangular mesh. Following Green's second identity, the potential $\phi(\mathbf{x})$ at any point $\mathbf{x}$ of the thoracic domain is given as

$$\phi(\mathbf{x}) = \frac{1}{4\pi}\int_{S_B}\phi_B\frac{\mathbf{r}\cdot\mathbf{n}}{||\mathbf{r}||^3}dS_B - \frac{1}{4\pi}\int_{S_H}\left[\phi_e\frac{\mathbf{r}\cdot\mathbf{n}}{||\mathbf{r}||^3}+\frac{\nabla\phi_e\cdot\mathbf{n}}{||\mathbf{r}||}\right]dS_H \tag{3.11}$$

where subscripts B denote the body surface and the potentials thereupon, S_H the epicardial heart surface, and $\mathbf{n}$ the surface normal unit vector facing outward of the domain under consideration (i.e. outward at the torso and inward at the epicardium). The vector $\mathbf{r}$ is defined by $\mathbf{x}$ and the integration point. Note that equation 3.11 assumes that $\nabla\phi_B = 0$.

By positioning an observer point on each of these surfaces as illustrated in fig. 3.6 (a) for the heart surface, separate equations for the two locations can be written:

$$-\phi_B^i + \frac{1}{4\pi}\int_{S_B}\phi_B\,d\Omega_{BB}^i - \frac{1}{4\pi}\int_{S_H}\phi_e\,d\Omega_{BH}^i - \frac{1}{4\pi}\int_{S_H}\frac{\nabla\phi_e\cdot\mathbf{n}}{||\mathbf{r_i}||}dS_H = 0 \tag{3.12}$$

$$\frac{1}{4\pi}\int_{S_B}\phi_B\,d\Omega_{HB}^i - \phi_e^i - \frac{1}{4\pi}\int_{S_H}\phi_e\,d\Omega_{HH}^i - \frac{1}{4\pi}\int_{S_H}\frac{\nabla\phi_e\cdot\mathbf{n}}{||\mathbf{r_i}||}dS_H = 0 \tag{3.13}$$

Using the same subscripts as above to specify heart and torso surfaces, equations 3.12 and 3.13 were simplified by introducing the notion of solid angle $d\Omega_{ef}^i$, i.e. the solid angle subtended by surface element dS_f at the i-th location of surface e:

$$d\Omega_{ef}^i = \frac{\mathbf{r_i}\cdot\mathbf{n}}{||\mathbf{r_i}||^3}\,dS_f \tag{3.14}$$

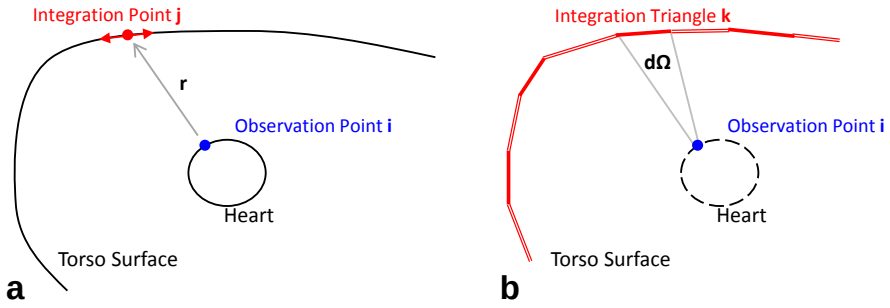

Figure 3.6: **a)** Schematic of torso and heart surfaces showing observation and integration points. **b)** After discretization, the surface is represented by triangles spanning solid angles $d\Omega$. *See text for details.*

Thus, the first subscript in all solid angle notations defines the surface where the observer is placed, and the second subscript the surface of integration. Special care has to be taken if both surfaces are identical ($d\Omega_{HH}$ and $d\Omega_{BB}$), because this will raise the situation that the observation point is one of vertices of the integration triangle.

After discretization and reformulation in matrix form, the following linear system can constructed:

$$\mathrm{P}_{BB}\,\phi_B + \mathrm{P}_{BH}\,\phi_e + \mathrm{G}_{BH}\,\Gamma_H = 0 \tag{3.15}$$

$$\mathrm{P}_{HB}\,\phi_B + \mathrm{P}_{HH}\,\phi_e + \mathrm{G}_{HH}\,\Gamma_H = 0 \tag{3.16}$$

Hereby, the matrix Γ_H contains the gradients $\nabla\phi_e$ and cancels out when the system is solved. The coefficients of matrices P and G entirely depend on the geometry, and by defining a completely precomputable transfer matrix

$$\mathrm{Z}_{BH} = \left(\mathrm{P}_{BB} - \mathrm{G}_{BH}\mathrm{G}_{HH}^{-1}\mathrm{P}_{HB}\right)^{-1}\left(\mathrm{G}_{BH}\mathrm{G}_{HH}^{-1}\mathrm{P}_{HH} - \mathrm{P}_{BH}\right) \tag{3.17}$$

the potentials on the body are given by $\phi_B = \mathrm{Z}_{BH}\,\phi_e$ [6]. Computing the matrix Z_{BH} hence requires two matrix inversions, for which the Eigen library[2] was used.

To obtain the geometric coefficients of matrices P and G, the integrals are calculated in a vertex-to-triangle fashion as shown in fig. 3.6 (b). For instance, the coefficient $P_{HB_{ij}}$ is obtained by first placing the observer at the i-th vertex of the heart surface. Then, all the triangles $k \in \mathbf{C}_j$ are iterated, where $\mathbf{C}_j$ is the close region of j, i.e. the set of all triangles directly around the j-th vertex of the body surface:

$$P_{HB_{ij}} = \frac{1}{3}\sum_{k\in\mathbf{C}_j} d\Omega_{ik} \tag{3.18}$$

Computing the coefficients of matrices P is straightforward because there is a closed-form formula available for solid angles in tetrahedra. The surface over distance integrals of matrices G are more challenging; Gaussian quadrature of order 6 was a good compromise between precision and runtime performance.

[2]Eigen C++ library for linear algebra, `http://eigen.tuxfamily.org`

3.3.3 Electrocardiogram Calculation

From the potentials ϕ_B at the torso, the standard Einthoven, Goldberger and Wilson leads (as described in section 1.3.3) are computed. For the subsequent calibration of diffusion coefficients, two features of the ECG signals instead of the entire ECG traces are utilized: The duration of the QRS complex Δ_{QRS} intuitively signifies the total time the electrical wave requires to propagate throughout the entire myocardium, and the mean electrical axis angle α allows the detection of imbalances between left and right ventricular wave conduction. Because these two features are automatically derived by ECG devices in clinical routine and printed on ECG recordings, calibration using the trained regression model is simple and does not require digitized ECG traces. From the computed ECG signals, Δ_{QRS} and α are derived automatically following the algorithm outlined in [43]:

1. Denoting the various limb lead signals as $y(t)$, filtered signals $y_f(t)$ are computed by squaring the respective derivatives:
$$y_f(t) = \left[\frac{d}{dt}y(t)\right]^2 \tag{3.19}$$
2. Next, $y_f(t)$ is convolved with a sliding average kernel of window size $24\,ms$ for increased robustness:
$$y_c(t) = y_f(t) \star \left(\frac{1}{N}[1\,1\,\ldots\,1\,1]\right) \tag{3.20}$$
3. A threshold value $\tau = 0.8\,mV^2ms^{-2}$ has proven to be sufficient for detecting the QRS complex and its duration Δ_{QRS} for a given, single heart cycle,
$$y_t(t) = \begin{cases} 1, & \text{if } y_c(t) \geq \tau \\ 0, & \text{otherwise} \end{cases} \tag{3.21}$$
$$\Delta_{QRS} = \frac{1}{f_S}\sum y_t(t) \tag{3.22}$$
where f_S is the sampling frequency.
4. Finally, the electrical axis is calculated based on the leads I and II:
$$\alpha = \arctan\frac{2h_{II} - h_I}{\sqrt{3}h_I} \tag{3.23}$$
Hereby, the h_i's are the sum of R and S peak amplitudes in the respective leads.

3.3.4 Data-Driven Diffusion Calibration

The forward EP and ECG model as described above, i.e. computing ECG signals and parameters from a specific model of anatomy and EP, can be seen as a dynamic system $\mathbf{y} = f(\theta)$. In this thesis, the free parameters of f are the diffusion parameters, and the system's outputs are the ECG parameters:
$$\begin{pmatrix}\Delta_{QRS}\\ \alpha\end{pmatrix} = f\begin{pmatrix}c_{Myo}\\ c_{LV}\\ c_{RV}\end{pmatrix} \tag{3.24}$$

Model calibration thus consists of evaluating a function $g(\mathbf{y})$ that approximates the inverse problem $\theta = g(\mathbf{y}) \approx f^{-1}(\mathbf{y})$. Figure 3.7 schematically illustrates inputs and outputs of our regression model.

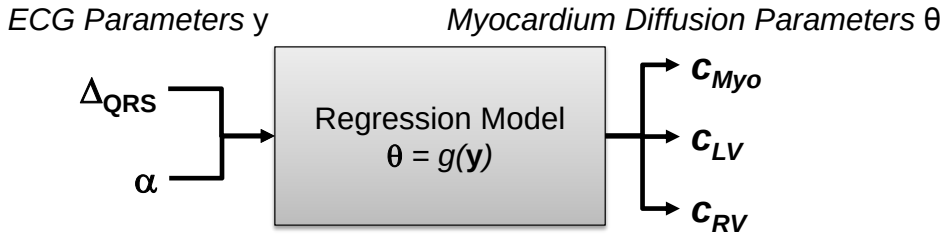

Figure 3.7: Schematic illustration of the data-driven regression model.

Normalization of Δ_{QRS} and α is necessary because of significant variation within the population, even in healthy subjects, due to heart morphology, position, and other factors not directly related to myocardium diffusivity. Therefore, we run three forward EP simulations for each patient with the diffusivity parameters listed in table 3.1.

Configuration F_1 includes nominal EP diffusion parameters and thus entails a normal wave propagation. Intuitively encoding the overall heart size (provided same diffusivity, the electrical wave will take longer to propagate through the entire myocardium in larger hearts), we use $\Delta_{QRS_{F_1}}$ to normalize the QRS duration Δ_{QRS}:

$$\overline{\Delta_{QRS}} = \left(\frac{\Delta_{QRS}}{\Delta_{QRS_{F_1}}} \right) \tag{3.25}$$

The others two configurations contain low LV diffusivity (LBBB-like scenario, F_2) and low RV diffusivity (RBBB-like scenario, F_3). Simulations with F_2 and F_3 scope the entire space of α of one particular patient, which allows, intuitively, to decide whether a specific electrical axis α expresses a left or right axis deviation. Normalization is performed as follows:

$$\overline{\alpha} = \left(\frac{\alpha - \alpha_{F_2}}{\alpha_{F_3} - \alpha_{F_2}} \right) \tag{3.26}$$

As a result, a set of normalized parameters $(\overline{\Delta_{QRS}}, \overline{\alpha})$ intrinsically considers patient geometry features.

Configuration	c_{Myo} (mm^2/s)	c_{LV} (mm^2/s)	c_{RV} (mm^2/s)
F_1	6,000	16,000	16,000
F_2	1,000	1,200	16,000
F_3	1,000	16,000	1,200

Table 3.1: Forward simulation diffusion configurations. *See text for details.*

Finally, the model $\theta = g(\overline{\Delta_{QRS}}, \overline{\alpha})$ is learned using the multivariate polynomial regression method [31]. Degree seven offered a good compromise between prediction accuracy and generalization, as no significant differences in performance with degrees varying from

4 to 9 could be distinguished. One regression function is learned for each diffusivity parameter independently, $\mathbf{g} = (g_{Myo}, g_{LV}, g_{RV})$. Multivariate regression splines (MARS) and gradient boosting [31] were also investigated, yielding very similar results.

After training of $\mathbf{g}$, the diffusivity parameters are estimated using measured and normalized ECG features:

$$\begin{pmatrix} c_{\hat{Myo}} \\ c_{\hat{LV}} \\ c_{\hat{RV}} \end{pmatrix} = \begin{bmatrix} g_{Myo} \\ g_{LV} \\ g_{RV} \end{bmatrix} \begin{pmatrix} \overline{\Delta_{QRS}} \\ \overline{\alpha} \end{pmatrix} \tag{3.27}$$

3.4 Cardiac Biomechanics and Hemodynamics

3.4.1 Finite Element Framework

Cardiac biomechanics and hemodynamics are computed using the finite-element method (FEM) on linear tetrahedra meshes. In the central dynamics equation,

$$\mathrm{M}\ddot{\mathbf{u}} + \mathrm{C}\dot{\mathbf{u}} + \mathrm{K}\mathbf{u} = \mathbf{F}_a + \mathbf{F}_p + \mathbf{F}_b \tag{3.28}$$

$\ddot{\mathbf{u}}$, $\dot{\mathbf{u}}$ and $\mathbf{u}$ gather the accelerations, velocities and displacements of the mesh nodes. M is the mass matrix, K the internal elastic stiffness matrix and C the (Rayleigh) damping matrix. The force vectors $\mathbf{F}_a$, $\mathbf{F}_p$ and $\mathbf{F}_b$ model active stress (cardiac contraction), ventricular blood pressure and mechanical boundary conditions, respectively, and are described in detail in the following sections.

The dynamics equation can be approximated using an implicit Euler scheme [5], allowing larger time steps and higher numerical stability than explicit schemes. In this thesis, a time step of $1ms$ was used. The resulting linear system $\Xi\mathbf{u} = \mathbf{F}$ is solved using the conjugate gradient method. In general, all components of the dynamics equation (3.28) are embedded in the SOFA framework[3].

3.4.2 Passive Stress

In this work, quantities of the biomechanic model are formulated in a total Lagrangian framework [55], where all variables are referred to the original configuration of the system. This allows the precomputation of variables and parallel execution of nearly all calculations.

The basic deformation variable for the description of the local kinematics in linear tetrahedra meshes is the deformation gradient F. Using tetrahedron shape vectors $\mathbf{D}_i$ as the cross product of two opposing edges respectively [52], the deformation gradient is written as

$$\mathrm{F} = \sum_{i=0}^{4} \mathbf{x}_i \, \mathbf{D}_i \tag{3.29}$$

[3] Simulation Open Framework Architecture [1], `http://www.sofa-framework.org`

where vectors $\mathbf{x}_i$ denote the current nodal positions in each time step. Associated with F are (1) the Jacobian determinant $J = \det(\mathrm{F})$, which quantifies the volume variation and can be expressed as closed form formula solely depending on the vertex positions [52], (2) the right Cauchy-Green deformation tensor $\mathrm{C} = \mathrm{F}^\intercal\mathrm{F}$, and (3) the left Cauchy-Green deformation tensor $\mathrm{B} = \mathrm{F}\mathrm{F}^\intercal$.

The passive tissue properties are modeled using the orthotropic Holzapfel-Ogden (HO) model [33], which uses the following invariants of the right Cauchy-Green deformation tensor C (unit vectors $\mathbf{a}$ and $\mathbf{b}$ are preferred material directions):

$$I_1 = tr\,\mathrm{C} \qquad I_4 = \mathbf{a}\cdot(\mathrm{C}\,\mathbf{a}) \qquad I_8 = \mathbf{a}\cdot(\mathrm{C}\,\mathbf{b}) = \mathbf{b}\cdot(\mathrm{C}\,\mathbf{a}) \tag{3.30}$$

While I_1 is a principal invariant, I_4 and I_8 introduce anisotropy in different directions, and a coupling between them. In the HO model, the fiber direction $\mathbf{f}$ and the fiber sheet direction $\mathbf{s}$ are used as $\mathbf{a}$ and $\mathbf{b}$ (invariants I_{4f}, I_{4s} and I_{8fs}).

The strain-stress energy function of the HO model consists of five parts and writes:

$$\begin{aligned}\Psi = &\frac{a}{2b}exp\left[b(I_1-3)\right]\\ &+\mathcal{H}_\delta(I_{4f}-1)\frac{a_f}{2b_f}\left\{exp\left[b_f(I_{4f}-1)^2\right]-1\right\}\\ &+\mathcal{H}_\delta(I_{4s}-1)\frac{a_s}{2b_s}\left\{exp\left[b_s(I_{4s}-1)^2\right]-1\right\}\\ &+\frac{a_{fs}}{2b_{fs}}\left[exp(b_{fs}I_{8fs}^2)-1\right]\\ &+D_1(J-1)^2\end{aligned} \tag{3.31}$$

The a_k's and b_k's are material constants. a and b correspond to the first, isotropic term, subscripts f to the anisotropic term in fiber direction, subscripts s to the anisotropic term in fiber sheet direction, and subscripts fs to the anisotropic term in transverse sheet direction. All a parameters have the dimension of stress, whereas all b parameters are dimensionless. $\mathcal{H}_\delta(\cdot)$ is the logistic function, a smooth approximation of the Heaviside step function employed here for increased numerical stability. Finally, D_1 is a parameter equivalent to the bulk modulus.

To improve computation efficiency, the strain-stress energy function is expressed according to the Multiplicative Jacobian Energy Decomposition (MJED) formulation [52]:

$$\Psi = \sum_k f^k(J)g^k(\tilde{I}) \tag{3.32}$$

The idea is to decompose the energy function such that g^k is independent of J and only depends on the invariants $\tilde{I} = [I_1, I_{4f}, I_{4s}, I_{8fs}]$. Thus, its derivative will not involve any costly matrix inversions. Eventually, the nodal forces $\mathbf{F}_i$ and the edge stiffness matrices K_{ij} ($\mathbf{x}_i$ and $\mathbf{x}_j$ are two connected nodes) are defined as follows:

$$\mathbf{F}_i = -\frac{\partial\Psi}{\partial\mathbf{x}_i} \qquad \mathrm{K}_{ij} = \frac{\partial^2\Psi}{\partial\mathbf{x}_i\partial\mathbf{x}_j} \tag{3.33}$$

Following these definitions, the derivation of Ψ consists of first computing $\partial f^k(J)/\partial \mathbf{x}_i$, for which closed form expressions that do not involve calculating C^{-1} are available [52]. Second, deriving $g^k(\tilde{I})$ requires calculating their first and second derivative with respect to C, which can be easily calculated through the identities given above (eqq. 3.30).

3.4.3 Active Stress

The active contraction forces $\mathbf{F}_a$ of the dynamics equation 3.28 couple the electrophysiology model with the biomechanic model. In this work, the computation of cardiac EP is performed beforehand on end-diastasis geometry. From the EP simulation, two parameters are obtained for each vertex of the tetrahedral mesh: The depolarization time T_d, defined as the point in time when the transmembrane action potential exceeds the changeover voltage v_{gate}, and the repolarization time T_r, defined as the point in time when the potential drops back below v_{gate}.

Expressing the active Cauchy stress tensor σ_c in terms of the action potential, the model proposed in [81] is then used to integrate myocardial contractility into the framework. The model is based on the following ODE ($\dot{\sigma_c}$ is the time derivative of σ_c):

$$\dot{\sigma_c} + \sigma_c = u\,\sigma_0 \tag{3.34}$$

Hereby, $u \in [0;1]$ is the normalized action potential, and σ_0 the maximum contraction stress that can be reached by a cell. To avoid time stepping, u is replaced by the values 0 and 1 for depolarization and repolarization, which allows to write σ_c in closed form. During depolarization ($T_d \leq t \leq T_r$), the stress tensor writes:

$$\sigma_c(t) = \sigma_0 \left(1 - e^{k_{ATP}(T_d - t)}\right) \tag{3.35}$$

During repolarization ($T_r < t < T_d +$ heart period), the stress tensor is defined as:

$$\sigma_c(t) = \sigma_c(T_r)\, e^{k_{RS}(T_r - t)} = \sigma_0 \left(1 - e^{k_{ATP}(T_d - T_r)}\right)\, e^{k_{RS}(T_r - t)} \tag{3.36}$$

The rates, which control the contraction stress increase and decrease, are the ATP binding rate k_{ATP} and the release rate k_{RS}. Together with σ_0, they form the main parameters of the model and be defined globally (in this work k_{ATP} and k_{RS}) or locally for each mesh node (in this work σ_0, to allow stronger LV contraction and suppress contraction of the connective tissue close to the valves).

Finally, the contraction stress needs to be integrated over the tetrahedral elements and expressed as force vector [81]:

$$\mathbf{F}_a = \int_V div\left(\sigma_c \mathbf{f} \otimes \mathbf{f}\right) dV = \int_S \left(\sigma_c \mathbf{f} \otimes \mathbf{f}\right) \mathbf{n}\, dS \tag{3.37}$$

In this equation, $\mathbf{f}$ denotes the fiber direction, $\otimes$ the tensor product and the term $\sigma_c\, \mathbf{f} \otimes \mathbf{f}$ the 3D contraction stress tensor. The force is equivalent to a pressure applied along the fiber orientation, and is computed for each triangle of each tetrahedron using the surface normal vectors $\mathbf{n}$.

3.4.4 Mechanical Boundary Conditions

Two mechanical boundary conditions are considered:

$$\mathbf{F}_b = \mathbf{F}_{spr} + \mathbf{F}_{peri} \tag{3.38}$$

First, the effect of arteries and atria on ventricular motion is modeled by connecting the valve plane vertices to springs [81] with anisotropic stiffness K such that radial motion is permitted. Valve plane vertices are automatically defined as endocardium border vertices. The fixed extremity of the springs corresponds to the rest position of the nodes $\mathbf{x}_0$, taken at diastasis when the heart is still at rest. The contributions of the springs are gathered into the force vector $\mathbf{F}_{spr}$:

$$\mathbf{F}_{spr}(\mathbf{x}) = \mathrm{K}\ (\mathbf{x} - \mathbf{x}_0) \tag{3.39}$$

The anisotropic stiffness K is obtained by

$$\mathrm{K} = [\mathbf{e}_l\, \mathbf{e}_r\, \mathbf{e}_c] \begin{pmatrix} k_l & 0 & 0 \\ 0 & k_r & 0 \\ 0 & 0 & k_c \end{pmatrix} [\mathbf{e}_l\, \mathbf{e}_r\, \mathbf{e}_c]^{-1} \tag{3.40}$$

where $[\mathbf{e}_l\, \mathbf{e}_r\, \mathbf{e}_c]$ is the transformation matrix from the global coordinate system to the coordinate system defined by the long axis $\mathbf{e}_l$ and the short axis plane $(\mathbf{e}_r, \mathbf{e}_c)$ as illustrated in fig. 3.8 (left panel). Parameters k_l, k_r, and k_c define the spring stiffness in the respective directions.

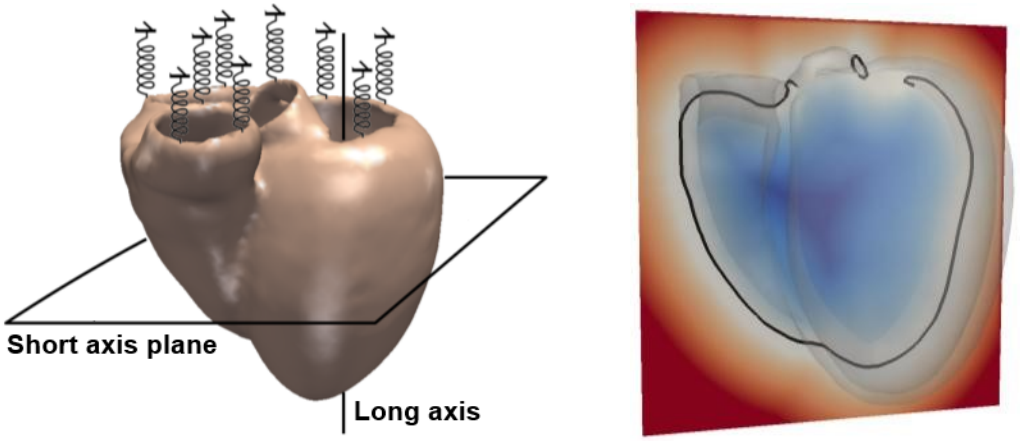

Figure 3.8: Mechanical boundary conditions. **Left panel**: Springs attached to the valve plane vertices model the effect of arteries and atria on the ventricles. Image from [47], modified. **Right panel**: Distance map used to compute the pericardium force. Red regions are outside of the pericardial bag and form a restricted zone for endocardial nodes.

Second, the heart motion is also constrained inside the pericardium bag and by the neighboring lungs and liver. These interactions are modeled using the contact-based pericardium constraint proposed in [47]. Let $\delta\Omega$ be the pericardium, defined by the epicardium

at end-diastole. A distance map $D_{\delta\Omega}$, as shown in fig. 3.8 (right panel), is computed from Ω, with $D_{\delta\Omega} < 0$ inside the pericardial bag. We then add to the epicardial nodes the force

$$\mathbf{F}_{peri}(\mathbf{x}) = \begin{cases} k\dfrac{(D_{\delta\Omega}(\mathbf{x}) - d_{out})^2}{(D_{\delta\Omega}(\mathbf{x}) - d_{out})^2 + m^2}\nabla D_{\delta\Omega}(\mathbf{x}), & \text{if } D_{\delta\Omega}(\mathbf{x}) > d_{out} \\ -k\dfrac{(D_{\delta\Omega}(\mathbf{x}) - d_{in})^2}{(D_{\delta\Omega}(\mathbf{x}) - d_{in})^2 + m^2}\nabla D_{\delta\Omega}(\mathbf{x}), & \text{if } D_{\delta\Omega}(\mathbf{x}) < d_{in} \\ 0, & \text{otherwise} \end{cases} \tag{3.41}$$

The parameters d_{out} and d_{in} (dilation parameters of the pericardium bag), k (contact force amplitude) and m (contact force rate) control where the force starts to apply, its maximum strength and how fast it is reached. If the displacement of an epicardial node exceeds d_{out}, a force to push it back perpendicularly is induced, creating a restricted zone outside the pericardial bag. The impact of inward radial displacement is controlled by d_{in}, reducing the motion of the epicardium compared to the one of the endocardium. As the gradient of the distance map $\nabla D_{\delta\Omega}$ defines the magnitude of the force, friction-free sliding between myocardium and pericardium is ensured.

3.4.5 Hemodynamics

For a complete model of heart biomechanics, consideration of blood hemodynamics is essential. As the ventricular blood exerts its pressure on the myocardial walls, cardiac contraction antagonizes the remote pressure in pulmonary and systemic circulation, and the damping in aorta and arteries. The valves enforce unidirectional blood flow, and their opening and closing governs the transition between the four cardiac phases illustrated in figure 3.9.

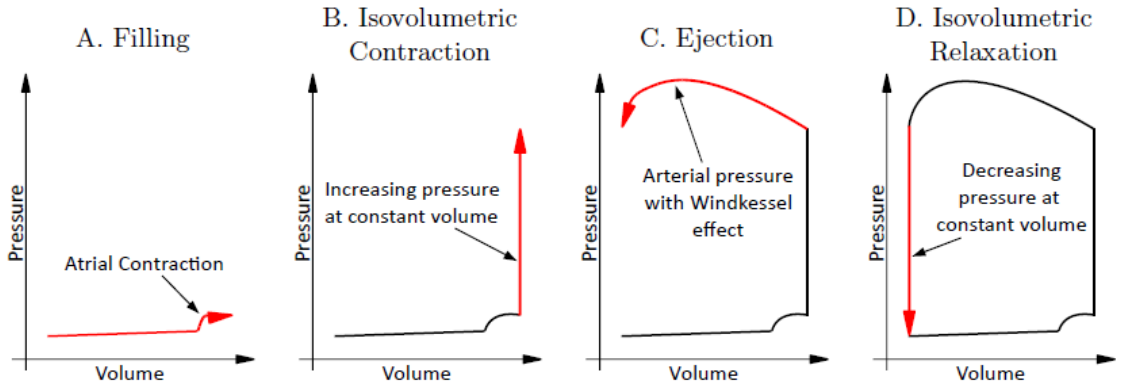

Figure 3.9: Overview of the four cardiac phases. Image from [47].

In this work, ventricular pressure p is added to the dynamics system (eq. 3.28) using the nodal forces

$$\mathbf{F}_p = p\,\mathbf{N} \tag{3.42}$$

As pressure is defined as force per area, exerted perpendicularly, the vector $\mathbf{N}$ needs to gather both surface areas and normals. Let T_e be the triangulated endocardial surface, the

notion $t \in T_e$ adj i signifies all surface triangles t that are adjacent to vertex i.

$$\mathbf{N}_i = \frac{1}{3} \sum_{t \in T_e \text{ adj } i} \left(\mathbf{n}_t \int_t dS \right) \tag{3.43}$$

The computation of pressure p is dependent on the current cardiac phase. The following sections will describe the utilized models for each phase respectively. As the simulation passes through the different phases, the models and their boundary conditions are applied in an alternating fashion.

Atrium Model

During filling, blood enters the ventricles through the atrioventricular valves and the ventricular blood flow q, defined as the derivative of the chamber volume $Q = d/dt\, V$, is positive. Accordingly, the ventricular pressure is equal to the atrial pressure. Modeling atrial contraction may be computationally demanding, and this work focuses on ventricular contraction. Therefore, a simplified phenomonological model of atrial blood pressure as proposed in [41] is used. Neglecting pulmonic and systemic circulations, the model decouples the atria from the arteries. The following, lumped time-varying elastance model describes the atrial pressure p_A:

$$p_A = E\,(V_A - V_{A,rest}) \tag{3.44}$$

$$E = (E_{max} - E_{min})\gamma_a + E_{min} \tag{3.45}$$

$$V_{A,rest} = (1 - \gamma_a)(V_{rd} - V_{rs}) + V_{rs} \tag{3.46}$$

$$\gamma_a = \begin{cases} -12\cos(2\pi t_{atrium}/t_{twitch}) + 0.5, & \text{if } t_{atrium} < t_{twitch} \\ 0, & \text{if } t_{atrium} \geq t_{twitch} \end{cases} \tag{3.47}$$

$$t_{atrium} = \begin{cases} \mod\,(t - t_{active} + \Delta t_{PR}, t_{cycle}), & \text{if } t \geq t_{atrium} - \Delta t_{PR} \\ 0, & \text{if } t < t_{atrium} - \Delta t_{PR} \end{cases} \tag{3.48}$$

In these equations, minimum elastance E_{min}, maximum elastance E_{max}, diastolic volume at zero pressure V_{rd}, and systolic volume at zero pressure V_{rs} are free parameters of the model. γ_a is an activation function, where t_{twitch} is the duration of the ventricular contraction. t_{active} is the activation time of ventricular contraction, Δt_{PR} the duration of the PR interval, and t_{cycle} the duration of the heart cycle.

Finally, the atrial volume V_A is defined by the following ODE:

$$\frac{d}{dt}\, V_A = Q_{vein} - Q_{valve} \tag{3.49}$$

where Q_{valve} is the flow through the atrioventricular valve (equal to the variation in ventricular volume), and Q_{vein} the incoming flow through the pulmonary vein or the venae cavae:

$$Q_{vein} = \frac{p_{vein} - p_A}{R_{vein}} \tag{3.50}$$

Hereby, p_{vein} is the pressure in the vein (assumed constant), and R_{vein} the resistance of the vein. The equations are solved using a first-order Euler implicit scheme for numerical stability. Two independent models are used for the left and for the right atrium.

Arterial Model

During ejection, which is initiated when the ventricular pressure p reaches the arterial pressure, blood leaves the ventricles through the semilunar valves into the aorta and the pulmonary artery. Accordingly, the ventricular pressure is equal to the arterial pressure. In this work, a 3-element Windkessel model [94] is used to model arterial pressure. The model is based on electrical circuit analogies as shown in fig. 3.10, where the blood flow resembles electrical current, and pressure electrical voltage.

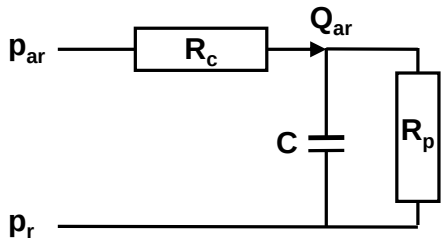

Figure 3.10: Circuit analogy of the 3-element Windkessel model.

The peripheral resistance R_p accounts for the distal resistance of the circulatory system, mainly due to small vessels and capillaries. The compliance C models the elasticity of the arterial walls. Finally, the characteristic resistance R_c incorporates the influence of the blood mass and the compliance of the artery proximal to the valves.

The following ODE defines the arterial pressure p_{ar}:

$$\frac{d}{dt}p_{ar}(t) = R_c\frac{d}{dt}Q_{ar}(t) + \left(1 + \frac{R_c}{R_p}\right)\frac{Q_{ar}(t)}{C} - \frac{p_{ar}(t) - p_r}{R_p\,C} \tag{3.51}$$

The arterial flow Q_{ar} is hereby defined as the opposite of the ventricular flow $Q_{ar} = -Q$, and the parameter p_r refers to the constant low pressure of reference, typically the pressure of the remote venous system. Again, this equation is integrated using a first-order Euler implicit scheme, and two independent models are used for aorta and pulmonary artery.

Isovolumetric Constraint

Between filling and ejection, both valves are closed. The myocardium contracts but due to the incompressibility of blood, the volume in the ventricle remains constant. The effect of muscle activity in this so-called isovolumetric phase is hence an increase of ventricular blood pressure. Similarly, between ejection and the next filling phase, the myocardium relaxes to reduce the blood pressure while maintaining the ventricular volume.

To keep the ventricular volume V constant during these phases, we propose an efficient projection-prediction isovolumetric constraint, which we enable during these phases. The idea is to find a pressure $\tilde{p}(t)$ that ensures $V(t + dt) = V_0$, where dt is the time step. Our method consists of three steps:

1. We solve the dynamic system (eq. 3.28) without constraint and compute unconstrained new vertex positions $\hat{\mathbf{x}}(t + dt)$.

2. The system is reformulated including an unknown corrective pressure $\lambda(t)$:

$$\Xi\mathbf{u}(t+dt) = \Xi(\mathbf{x}(t+dt) - \mathbf{x}_0) = \mathbf{F} + \lambda\mathbf{N} \tag{3.52}$$

Solving the system at $t + dt$ yields:

$$(\mathbf{x}(t+dt) - \mathbf{x}_0) = (\hat{\mathbf{x}}(t+dt) - \mathbf{x}_0) + \lambda\Xi^{-1}\mathbf{N} \tag{3.53}$$

The constrained system thus writes:

$$\begin{cases} \mathbf{x}(t+dt) = \hat{\mathbf{x}}(t+dt) + \lambda(t)\Xi^{-1}\mathbf{N} \\ V(t+dt) = V_0 \end{cases} \tag{3.54}$$

As shown in [73], the Lagrangian coefficient λ is computed by solving a third-order polynomial. The vertices are then projected by applying displacements $\mathbf{u}_p(t) = \lambda(t)\Xi^{-1}\mathbf{N}$.

3. Finally, the corrected pressure at the current time step is computed:

$$\tilde{p}(t) = p(t) + \lambda(t) \tag{3.55}$$

By utilizing a second-order Taylor expansion scheme, the pressure at the next time step is predicted:

$$p(t+dt) = \tilde{p}(t) + dt\frac{d\tilde{p}}{dt} + \frac{1}{2}dt^2\frac{d^2\tilde{p}}{dt^2} \tag{3.56}$$

$$= \frac{3}{2}\left[p(t) + \lambda(t)\right] - 2\tilde{p}(t-dt) + \frac{1}{2}\tilde{p}(t-2dt) \tag{3.57}$$

In contrast to the method proposed in [9], which solves the dynamics system three times, our algorithm only requires the system to be solved twice: To compute intermediate vertex positions $\hat{\mathbf{x}}(t+dt)$ and to compute the directions of the corrective displacements $\Xi^{-1}\mathbf{N}$.

3.4.6 Fast GPU Implementation

As the biomechanical submodels of our framework are the computationally most demanding ones, we focus our efforts on the the parallelization of these components. We use NVIDIA CUDA[4], version 5.5, as our development environment.

Solving the dynamics system of the biomechanics components involves the computation of nodal forces by accumulating the contributions of all elements sharing each node. Blood pressure forces, for instance, are first calculated per endocardial triangle, and subsequently accumulated and expressed per vertex. Table 3.2 gives an overview of computations that are not entirely vertex-wise and thus require accumulation of contributions.

Straightforward CPU implementations can avoid the accumulation by directly distributing the contributions. For the example of blood pressure forces mentioned above, this would translate into the following algorithm:

[4]Compute Unified Device Architecture, `http://developer.nvidia.com/cuda-toolkit`

1. Initialize nodal pressure force vectors $\mathbf{f}_i$ with 0.
2. Loop over all endocardial triangles, compute pressure force $\mathbf{F}$ using the triangle normal, and directly add it to the three involved vertices: $\mathbf{f}_i \leftarrow \mathbf{f}_i + \mathbf{F}/3$.

Unfortunately, the architecture of GPU devices does not allow such calculation schemes. Global random access accumulations are prohibited to avoid the racing condition that may emerge when different kernel threads write at the same shared memory. Instead, we propose an adaptation of the parallel implementation strategy proposed in [88] to efficiently solve the various components of our simulation framework.

Component	Quantity	Computed per	Contributions accumulated over
Passive Stress	Force	Vertex	Adjacent tetrahedra
	Edge Stiffness	Edge	Adjacent tetrahedra
	Force derivative	Vertex	Adjacent edges
Active Stress	Force	Vertex	Adjacent tetrahedra
Blood Pressure	Force	Vertex	Adjacent triangles

Table 3.2: Overview of computations that require accumulation of contributions. The computation of edge stiffnesses and force derivatives is due to the implicit Euler integration scheme used in the SOFA framework [5].

The key element of our method is the precomputed integer look-up table, *mapElements*, which is stored in a texture map for increased efficiency. Let V_{max} be the maximum valence of the mesh (maximum number of elements connected to a node), and N_n the number of nodes. *mapElements* is a table of size $2 \times N_n \times V_{max}$ that stores for any given node i the pairs (j, k), where j is the index of each adjacent element and k is the local index of that node in that element (e.g., $k \in [1, 4]$ if the element is a tetrahedron). Remaining positions, which occur when the node is shared by less than V elements, are initialized with a negative value (figure 3.11).

We then implement two kernels. First, a kernel *compute* is invoked across the N_e elements to perform the element-wise computation. It stores the element-wise contributions into separate floating point textures T^k of size N_e each. There are as many textures T^k as nodes shared by each element, for instance three for triangles and four for tetrahedra. Next, a kernel *accumulate* is invoked across N_n threads to accumulate element contributions to each node. This is achieved by looping over all V_{max} pairs (j, k) corresponding to the respective node and accumulating the element-wise contributions stored at the j-th positions of textures T^k. Figure 3.11 illustrates the texture *mapElements* and, for exemplary reasons, the first two textures T^k.

In contrast to [88], indexing of our look-up texture *mapElement* only requires the maximum valence, and not the actual nodal valence (which is not constant). We thus need to manage only one texture instead of two, resulting in simpler code but also in additional speed-up through texture alignment with the *accumulate* kernel threads. The higher memory demand, as shown in table 3.3, is negligible in the light of current GPU memory sizes.

The outlined method is employed to efficiently parallelize all computations listed in table 3.2. Other mechanical boundary conditions, such as the pericardium constraint, are formulated node-wise and therefore straightforward to implement in CUDA.

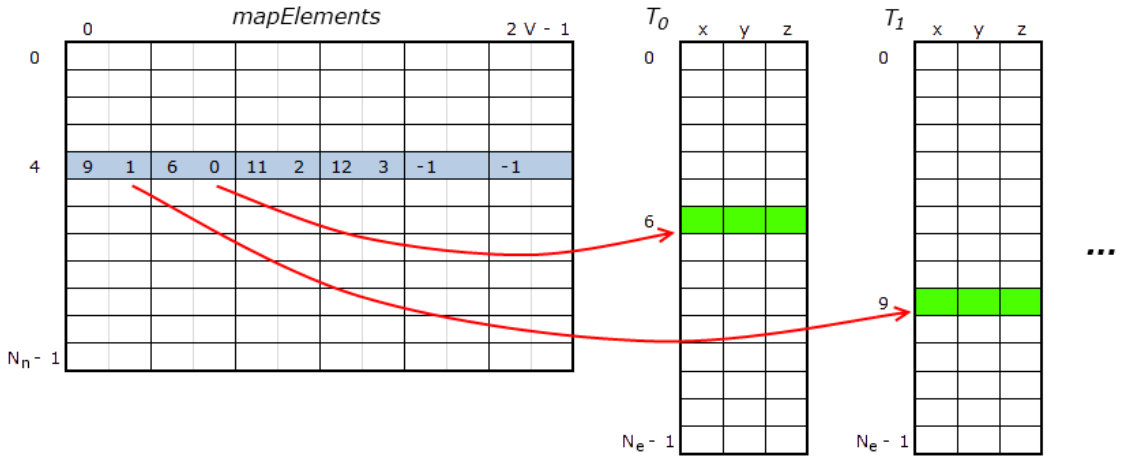

Figure 3.11: Example of contribution look-up texture: While the maximum valence is set to six, vertex no. 4 is shared by four elements (9, 6, 11 and 12), each involving a different node and thus a different texture T_i, of which only the first two are shown. Kernel *accumulate* will gather and accumulate the green contributions.

Mesh Elements	Texture size (proposed)	Texture size (Taylor)
200k	64.1 MB	24.4 MB
70k	22.4 MB	8.5 MB

Table 3.3: Memory demand of the proposed method compared to method of Taylor et al. [88] with maximum valence $V_{max} = 42$ and average valence $V_{avg} = 16$.

3.4.7 Personalization Procedure

In order to be predictive, personalization of the involved biomechanics and hemodynamics models of our framework needs to be performed. As already described, the anatomy model is generated from Cine MRI images and is thus inherently patient-specific. In addition to providing an anatomical model at end-diastasis, which is used for electrophysiology simulation and the initial state in the biomechanics model, the employed segmentation and tracking algorithm [100, 101] also allows to quantify the ventricular volume V in each MRI frame. As a result, it is possible to derive the following values:

- Function of ventricular flow over time: $Q(t) = V_t - V_{t-1}$
- Stroke Volume (SV), defined as the blood volume ejected during a single heart beat: $SV = EDV - ESV$, where EDV is the end-diastolic volume, and ESV the end-systolic volume.
- Ejection Fraction (EF), defined as the ratio between stroke volume and end-diastolic volume: $EF = SV/EDV$

The Windkessel models parameters for artery compliance are manually estimated based on the computed ventricular flow $Q(t)$ and invasively obtained pressure measurements

(ventricular and arterial pressures). We do not personalize the atrial models and use nominal values from the literature [41] instead.

Passive stress parameters of the biomechanics model are set as in [33]. The active stress and boundary condition parameters are manually estimated to match left ventricular ejection fraction (EF), stroke volume (SV) and visible cardiac motion. To reach a good personalization, dozens of simulations are necessary, which only becomes feasible due to the significant speed-up achieved by our GPU implementation.

3.5 Implementation Details

This section gives an overview which components of the presented framework were newly implemented in the course of this work, and which existing components could be utilized.

- As outlined in section 3.2, an existing C++ machine-learning framework [101] was used to segment and track heart anatomy from MRI images.
- An existing C++ toolbox for the rule-based assignment of fiber directions to the generated tetrahedral mesh was extended to correctly reflect state-of-the-art fiber sheet directions [7], including the presented Log-Euclidean orthonormal basis interpolation.
- In this work, an existing CUDA implementation of the LBM-EP algorithm [74] to compute transmembrane potentials was optimized and extended to also compute extracellular potentials [15] on the GPU.
- The boundary element solver [85] to map epicardial potentials to the torso, as well as the calculation of ECG signals was newly implemented in C++. The system relies on the Eigen library[5], a template library for linear algebra, to solve linear systems.
- Training and evaluation of the proposed data-driven regression framework to estimate myocardial diffusivity was newly implemented in MATLAB[6]. To allow interactive predictions, the trained regression model was integrated into the aforementioned C++ framework.
- All biomechanic and hemodynamic components of the dynamics equation presented in sec. 3.4 were embedded in the SOFA framework[7], an open source C++ software library and application for finite element simulations. The passive stress component (sec. 3.4.2) was newly implemented following the proposed GPU parallelization strategy. NVIDIA CUDA[8], version 5.5, served as development environment. Existing implementations of active stress and mechanical boundary conditions were significantly modified to also allow efficient GPU evaluation. While existing SOFA implementations of atrium and arterial blood pressure models were employed, the proposed isovolumetric constraint including the Taylor expansion-based pressure prediction was newly implemented.

[5] Eigen C++ library for linear algebra, `http://eigen.tuxfamily.org`
[6] MathWorks MATLAB, `http://www.mathworks.de/products/matlab`
[7] Simulation Open Framework Architecture [1], `http://www.sofa-framework.org`
[8] Compute Unified Device Architecture, `http://developer.nvidia.com/cuda-toolkit`

4 Experiments and Results

This chapter will report the results of all conducted experiments to evaluate the accuracy and computational performance of our modeling framework. First, benchmark experiments will shed light on the runtime performance of the various modeling components. Thereafter, our forward model of electrophysiology and electrocardiograms is qualitatively evaluated and the intrinsic uncertainty of diffusion parameters estimated. We evaluate our data-driven EP calibration model with both synthetic and real case datasets. An evaluation of the biomechanics and hemodynamics components concludes the chapter.

4.1 Experiment Data

The available datasets for our experiments were provided by our clinical partners from the University Hospital Heidelberg, Department of Internal Medicine III - Cardiology, Angiology and Pneumology, Heidelberg, Germany. We worked with the anonymized datasets of 13 patients suffering from dilated cardiomyopathy with subnormal to severely abnormal ejection fractions. Each dataset contained full heart cycle cine MRI images and heart catheter pressure measurements.

4.2 Benchmarks and Computational Performance

We evaluated the computational performance of our framework by running the entire simulation pipeline on one representative patient case. Our experiments were conducted on a system with a 16-core Intel Xeon 64-bit CPU at 2.4 GHz and an NVIDIA GeForce GTX 580 graphics card.

4.2.1 Cardiac Anatomy

The preparation times including the generation of the anatomical model are reported in table 4.1. All runtimes refer to purely CPU computations. The trend in runtime for mesh generation and anatomical model computation for different mesh resolutions (meshes with 24k, 43k, 64k, 127k and 274k tetrahedra) is reported in fig. 4.1 (left panel).

Task	CPU Runtime
MRI detection and tracking	$\approx$ 2 sec / frame
Tetrahedral mesh generation	64.4 sec
Anatomical model computation	16.8 sec

Table 4.1: Preparation and anatomical model generation times for a mesh with 64k elements.

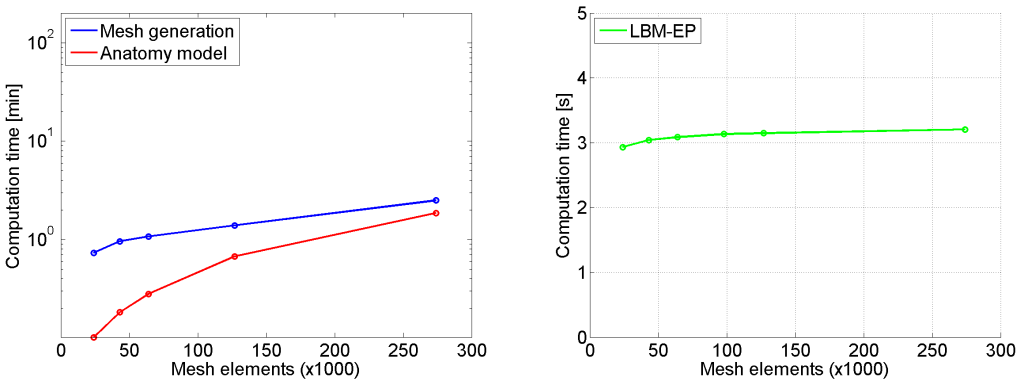

Figure 4.1: Performance comparison for different mesh resolutions. **Left panel**: Runtimes for mesh generation and anatomical model computation, reported in log-scale. **Right panel**: Runtimes for LBM-EP algorithm, using a $1.5 \times 1.5 \times 1.5\,mm$ grid.

4.2.2 Cardiac Electrophysiology

In table 4.2, the electrophysiology computation times using the LBM-EP algorithm are reported for different grid spacings. Fixing the computational domain to a Cartesian grid of $1.5 \times 1.5 \times 1.5\,mm$ and varying the mesh resolution, benchmark results as illustrated in fig. 4.1 (right panel) were obtained. All reported computation times include the calculation of extracellular potentials as required for the mapping to the torso.

Grid Spacing	GPU Runtime
1.5 mm	2.8 sec
0.7 mm	21.7 sec

Table 4.2: Runtimes of LBM-EP algorithm for different grid spacings.

The projection of the extracellular potentials to the torso and the derivation of the the ECG traces are simple matrix operations. Hence, the computation of the EP and ECG forward model can be done in **less than 3 seconds** for a grid with an isotropic resolution of 1.5 mm. Similarly, the evaluation of a learned polynomial regression function is far from being computationally expensive. The prediction of diffusion parameters for a patient thus requires **less than 10 seconds**, mainly because three forward runs for the purpose of normalization are needed.

4.2.3 Cardiac Biomechanics

For the evaluation of the biomechanics component of our framework, which is responsible for the most significant runtimes, we fixed the general system parameters reported in table 4.3. One full heart cycle, lasting 0.8 seconds, was computed in all subsequent experiments. Passive tissue parameters were set as in [33], and the active stress σ_0 was fixed at $150\,kPa$.

Table 4.4 reports the runtimes for two different meshes. For the mesh with 64k tetrahedra, the simulation only required 62 seconds, and even for the mesh with highest resolu-

Parameter	Value
Euler implicit time step	1 ms
Numerical threshold for CG solver	10^{-2} mm
Mass density	1.07 g/ml
Rayleigh damping coefficient (mass)	10^{4}
Rayleigh damping coefficient (stiffness)	10^{-1}

Table 4.3: Fixed biomechanic model parameters.

Tetrahedra	Avg. Edge Length	CPU Runtime	GPU Runtime	Speed-up
64k	2.9 mm	0:11:46.8 h	0:01:02.5 h	11.3x
274k	1.8 mm	1:26:23.4 h	0:10:12.0 h	8.5x

Table 4.4: CPU and GPU full heart cycle runtimes of the biomechanical components for two different mesh resolutions.

tion (274k), an entire heart cycle could be computed in 10 min and 12 seconds. On average, we gained a **mean speed-up factor of 10.6** (std. dev. 2.8) for different mesh resolutions (fig. 4.2, left panel). The overall runtime from image to model was **2 min and 31 seconds** for the mesh with 64k elements. Finally, scalability benchmarks on various graphics cards with 48, 192, 480 and 512 CUDA cores are shown in fig. 4.2 (right panel) for two different meshes.

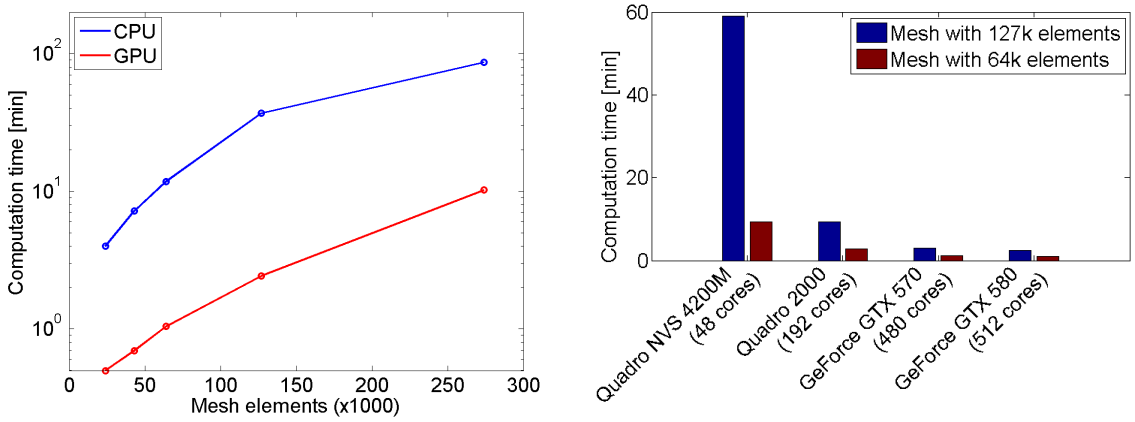

Figure 4.2: Biomechanic model performance benchmarks. **Left panel**: Comparison between CPU and GPU runtimes for different mesh resolutions in log-scale. **Right panel**: Scalability benchmarks showing GPU runtimes for two different meshes on various graphics cards [98].

4.3 Cardiac Electrophysiology

4.3.1 Experimental Protocol

For all 13 dilated cardiomyopathy patients, we generated a total of 4,200 EP simulations on a $1.5\,mm$ isotropic Cartesian grid. Diffusivity coefficients were uniformly sampled between $1,000\,mm^2/s$ and $16,000\,mm^2/s$ under the constraints $c_{Myo} \leq c_{LV}$ and $c_{Myo} \leq c_{RV}$ such that the Purkinje fibers in both ventricles conduct faster than the surrounding myocardium.

4.3.2 Forward ECG Model Evaluation

We evaluated our forward model of electrophysiology by running experiments with diffusion parameters listed in table 4.5. Normal EP was modeled with nominal diffusivity from literature, and a left bundle branch block (LBBB) scenario was modeled by reducing c_{LV} to $5,000\,mm^2/s$. Fig. 4.3 illustrates the computed Einthoven ECG leads V_I and V_{II} for both configurations.

Configuration	c_{Myo} (mm^2/s)	c_{LV} (mm^2/s)	c_{RV} (mm^2/s)
Normal	1,000	16,000	16,000
LBBB	1,000	5,000	16,000

Table 4.5: Diffusion parameters configurations for forward model evaluation.

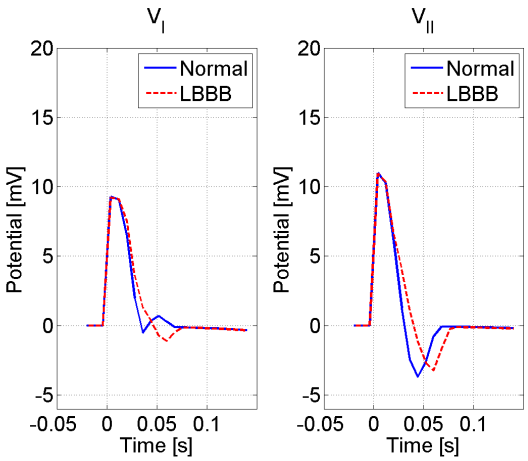

Figure 4.3: QRS complex in simulated limb ECG leads V_I and V_{II} in normal and left bundle branch block (LBBB) physiology [97].

4.3.3 Uncertainty Analysis

Based on the 4,200 simulations, we empirically estimated the uncertainty in diffusion parameters given a pair of Δ_{QRS} and α under our forward model. As the dataset contained simulations on different patient anatomies, normalized parameters were used for

this study to minimize the influence of geometry. All pairs of $(\overline{\Delta_{QRS}}, \overline{\alpha})$ were grouped in 20×20 bins, and for each bin, the standard deviation (SD) of c_{Myo}, c_{LV} and c_{RV} was calculated independently. Table 4.6 reports the total SD for the entire dataset, and the average local (bin-wise) SD relative to the total SD for c_{Myo}, c_{LV} and c_{RV}, respectively. As shown in fig. 4.4, the highest local uncertainty (up to 150% of total SD) is found in the healthy range of parameters, i.e. in the center of the plots.

	c_{Myo}	c_{LV}	c_{RV}
Total SD (entire dataset)	$2,146\,mm^2/s$	$4,142\,mm^2/s$	$4,123\,mm^2/s$
Average local SD in % of total SD	20%	52%	40%

Table 4.6: Total and local standard deviation (SD) in dataset of 4,200 EP simulations.

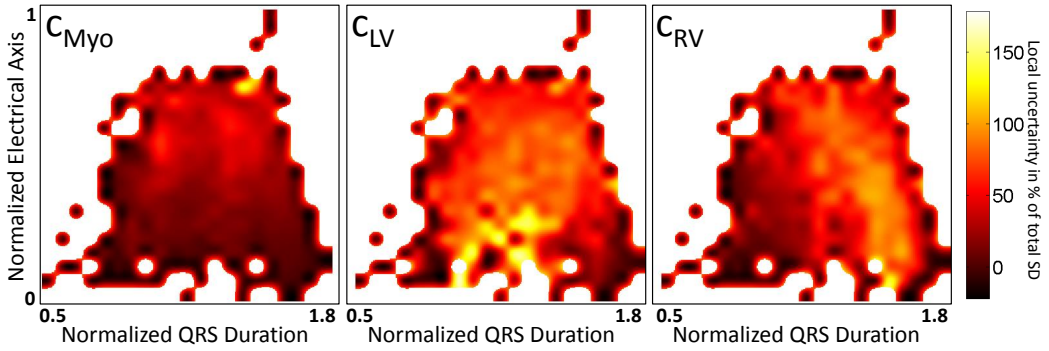

Figure 4.4: Empirical estimate of diffusion uncertainty [97].

4.3.4 Evaluation of the Calibration Model with Synthetic Data

We performed leave-one-patient-out cross-validation using the entire dataset of 4,200 simulations. Table 4.7 relates the average prediction error with the empirically estimated uncertainty reported in the previous section. Without normalization, errors were between 114% and 440% of the total standard deviation.

	c_{Myo}	c_{LV}	c_{RV}
Average prediction error	23%	56%	55%
Empirically estimated uncertainty	20%	52%	40%

Table 4.7: Average prediction error of leave-one-patient-out cross-validation, and estimated uncertainty for comparison. All figures in % of total standard deviation.

Next, we evaluated the accuracy of the regression model in the observable space of ECG parameters. For that purpose, we ran an additional forward simulation with the predicted diffusion coefficients, and compared Δ_{QRS} and α with the known ground truth. In order to assess the precision of the simulations obtained using our regression-based calibration method, we compared with two alternative methods:

- First, we compared with simulation results generated using nominal diffusion parameters from literature (configuration "Normal" in tab. 4.5).
- Second, we employed NEWUOA [72], a standard gradient-free inverse problem method, to predict diffusion parameters. The cost function was defined as follows:

$$f(\Delta^i_{QRS}, \alpha^i) = (\Delta^{known}_{QRS} - \Delta^i_{QRS})^2 + \lambda(\alpha^{known} - \alpha^i)^2 \tag{4.1}$$

Hereby, superscripts i denote the iteration index, and the weighting factor $\lambda = 0.1$ accounts for the different orders of magnitude between ECG parameters. Tissue diffusivities were estimated within 23%, 64% and 54% of the total SD for c_{Myo}, c_{LV} and c_{RV}, respectively. For each estimation, NEWUOA took about $10\,min$ to converge.

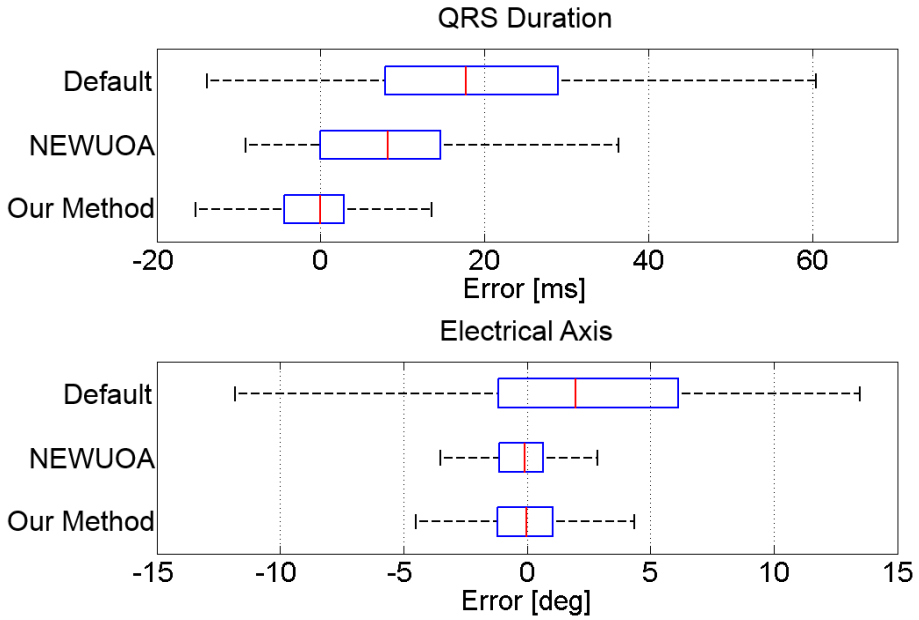

Figure 4.5: QRS duration and electrical axis error distributions for ECG simulations with nominal (top), NEWUOA-predicted (center) and regression-predicted (bottom) diffusivity parameters [97].

Error distributions for ECG simulations with nominal parameters, NEWUOA-predicted diffusion parameters, and diffusivities estimated using our proposed regression model are reported in fig. 4.5 and table 4.8. Calibrated simulations were significantly (t-test p-value < 0.001) more precise than those obtained with nominal diffusivity values. In addition, it should be noted that while our prediction was on average centered around the ground truth QRS duration (average bias: $+0.5\,ms$), the Δ_{QRS} calculated with default parameters was $19.0\,ms$ too short.

4.3.5 Evaluation of the Calibration Model on Real Cases

Finally, we evaluated our calibration method on four DCM patients, for which clinical ECG was available. Using the trained regression model, diffusivity coefficients were estimated

	QRS Duration Δ_{QRS} (ms)	Electrical Axis α (deg)
Default	19.8 ± 14.3	4.3 ± 3.4
NEWUOA	8.7 ± 11.1	-0.2 ± 7.6
Our Method	4.9 ± 5.5	1.6 ± 1.7

Table 4.8: Mean and standard deviation of QRS duration and electrical axis error distributions for ECG simulations with nominal, NEWUOA-predicted and regression-predicted diffusivity parameters.

based on measured QRS duration and electrical axis angle. In one case, myocardium diffusivity could not be predicted because the measured electrical axis ($\alpha = -63°$) was outside the range of the training set. However, we were able to obtain plausible diffusion coefficients ($2426 - 7584\,mm^2/s$ for c_{Myo}, and $6691 - 12532\,mm^2/s$ for c_{LV} and c_{RV}) for the other three patients. The average prediction error of the ECG using the calibrated forward model are reported in table 4.9. Figure 4.6 illustrates the calculated ECG overlaid on top of the real ECG for one patient.

	QRS Duration Δ_{QRS} (ms)	Electrical Axis α (deg)
Average error	0.35 ± 0.28	$15.6° \pm 9.6$

Table 4.9: Average prediction error for three real case simulations.

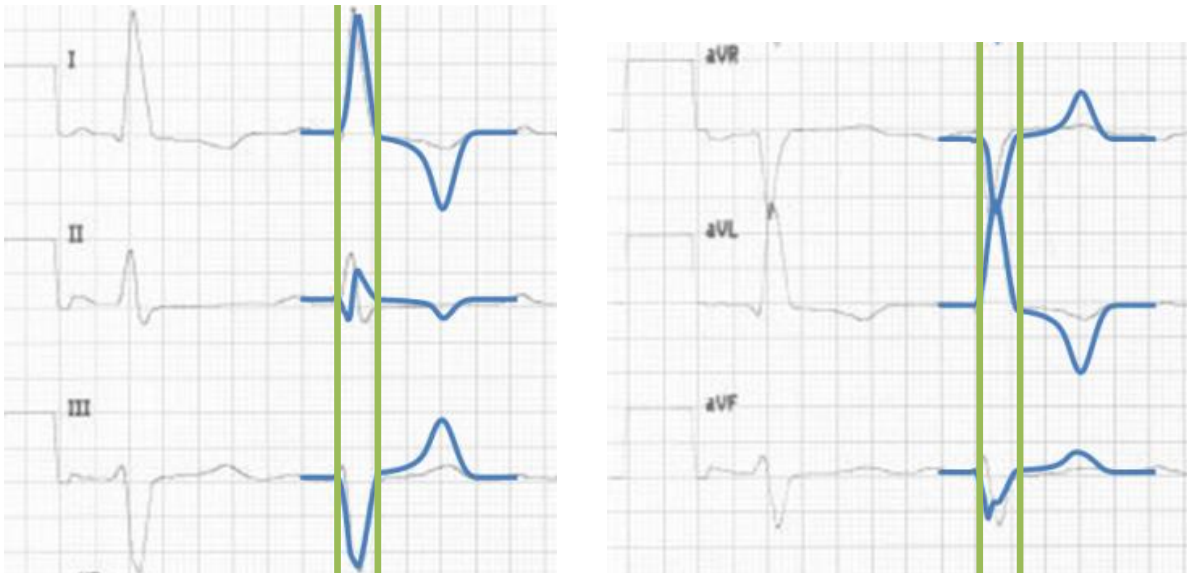

Figure 4.6: Measured (*black*) and simulated (*blue*) ECG leads after model calibration for one patient. The green bars highlight the QRS complex, which was subject to calibration.

4.4 Cardiac Biomechanics

4.4.1 Evaluation of Isovolumetric Constraint

The performance of the proposed constraint to keep the ventricular volume constant during isovolumetric phases is evaluated on one representative patient case. We computed cardiac EP using nominal diffusion parameters for one full heart cycle. The biomechanical simulation was run for two consecutive heart cycles, repeating EP signals triggering myocyte contraction with a period of $T = 0.8$ seconds.

In figure 4.7, we compared our approach with a penalty force defined by

$$\mathbf{F}_{pen}(t) = \int k_{iso} \left(V(t) - V_0\right) \mathbf{n} \, dS \tag{4.2}$$

where $V(t)$ is the ventricular volume at time t, and V_0 the ventricular volume at the beginning of the isovolumetric phase. The term $\mathbf{n}\, dS$ contains the lumped area vectors of the endocardial surface according to equations 3.42 and 3.43. Hence, the penalty factor k_{iso} can be understood as corrective pressure and is estimated manually for this experiment. The penalty force can be computed very efficiently, but does not necessarily ensure constant volume.

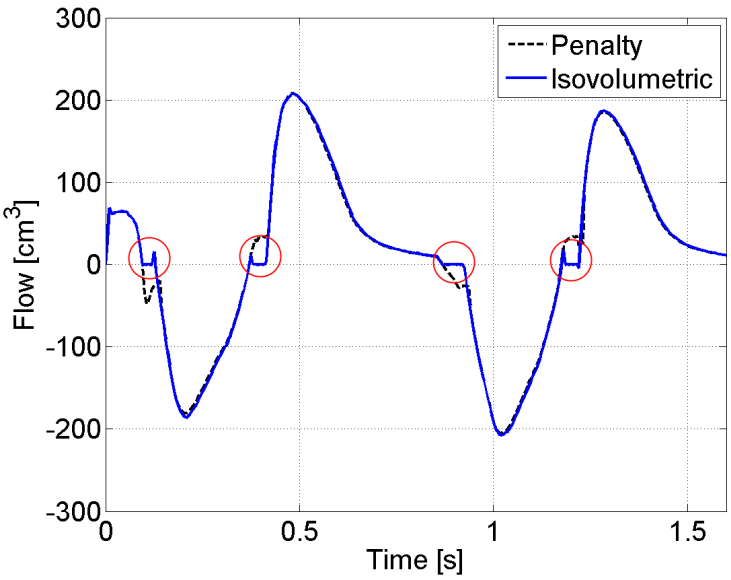

Figure 4.7: Left ventricular flow (change of volume) for two heart cycles, comparing the effectiveness of the proposed isovolumetric constraint with a penalty force method. The two methods only differ during isovolumetric phases as highlighted with red circles.

4.4.2 Evaluation on Real Cases

For five datasets of DCM patients, we manually personalized the biomechanical model as described in sec. 3.4.7 using the MRI images and catheter pressure measurements. In doing so, we tried to match the cardiac motion, left ventricular ejection fraction and stroke volume of each patient. For the electrophysiology, we also used nominal diffusion parameters in this experiment. Table 4.10 reports measured and computed ejection fractions and stroke volumes for all patients. For the patient with largest contraction, fig. 4.9 illustrates our personalized model overlaid on MRI slices, while fig. 4.8 shows the left ventricular pressure and volume over time.

Patient	EF_m	EF_c	SV_m (ml)	SV_c (ml)
1	41%	36%	106	91
2	14%	12%	40	33
3	27%	23%	67	56
4	15%	17%	71	80
5	34%	30%	85	66

Table 4.10: Comparison of left ventricular measured (EF_m) and computed (EF_c) ejection fractions, and measured (SV_m) and computed (SV_c) stroke volumes (in ml) for 5 cases.

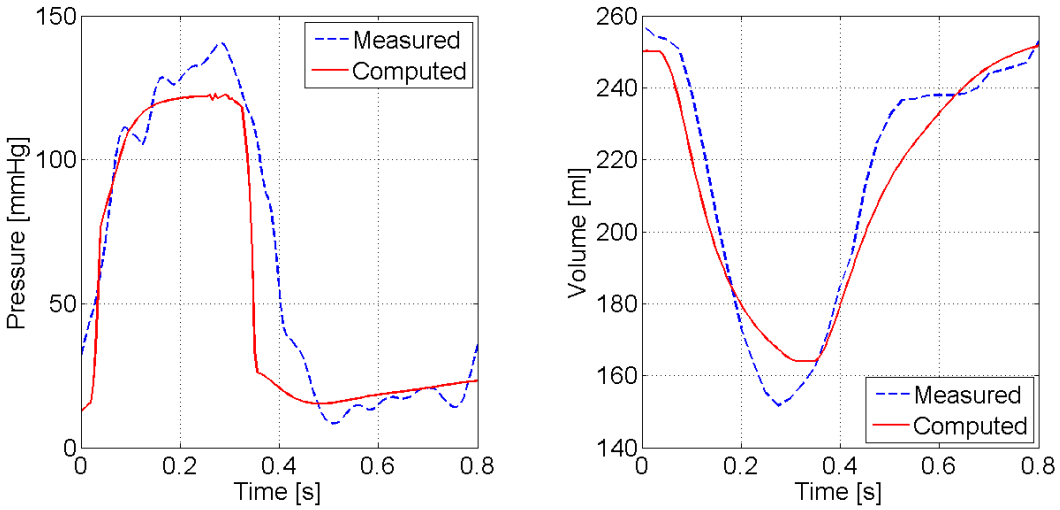

Figure 4.8: Personalization results for the patient with largest contraction. **Left panel** shows pressure curve and **right panel** volume curve for the left ventricle [98].

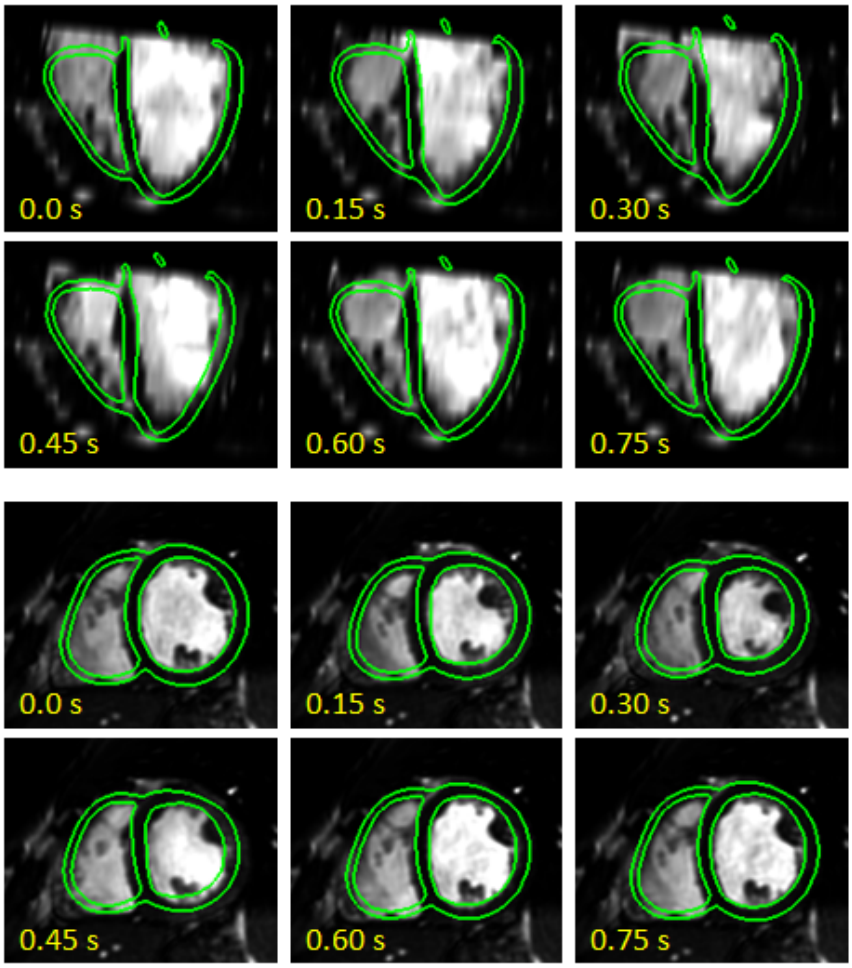

Figure 4.9: Personalization results for the patient with largest contraction. Long-axis (top) and short-axis (bottom) slices show MRI images and personalized model at various time steps throughout one heart cycle [98].

5 Discussion

While the previous chapter reported results from the conducted experiments, this chapter will discuss obtained findings. Interpretations of benchmark results on the computational performance will be followed by a thorough discussion of our evaluation results on the presented electrophysiology and biomechanics models.

5.1 Benchmarks Experiments

The conducted benchmark experiments are divided into three distinct parts: (1) The preparation and generation of the anatomical model, (2) the computation of cardiac electrophysiology, and (3) the simulation of cardiac biomechanics.

Regarding the preparation and anatomical model generation times, it should be noted that benchmark results are only reported for the sake of completeness. The focus of this work was laid on the cardiac electrophysiology and biomechanics components, therefore no special runtime optimization was performed. Also, due to the fact that these steps are only required once per patient, serial execution on the CPU was considered sufficient. The employed tracking and detection framework already performs fast, and for both the tetrahedral mesh generation and the computation of the anatomical model, parallelization optimizations for GPU architectures have the potential to improve the runtime performance significantly.

Results show that the computation times of the LBM-EP algorithm are independent of mesh resolution, which is not surprising as the method operates on Cartesian grids rather than tetrahedral elements. Runtimes of less than three seconds for the simulation of an entire heart cycle are near-real time and are a prerequisite for our data-driven regression model: Only because of this excellent runtime behaviour we could produce a large number of synthetic datasets for regression model training. Reported computation times indicate a speed-up of up to $40.5\times$ compared to a CPU implementation of the same algorithm. In total, the algorithm is between two and three orders of magnitude faster than current FEM-based approaches with meshes of comparable resolution [98]. We also consider the required time to calibrate the EP model for an unseen patient as clinically feasible.

The reported average speed-up factor of $10.6\times$ for the biomechancal model shows that the proposed GPU implementation strategy is able to sufficiently accelerate the model evaluation for a complete heart cycle such that user interaction with the model becomes possible, an essential requirement for applicability in clinical routine: Only the possibility to perform full heart cycle biomechanical simulations in a short time allows the extensive estimation of patient-specific model parameters. Also the overall runtime from image to biomechanical model is in the range of clinical feasibility. Regarding the scalability benchmarks, our results indicate that the computation time is linearly dependent on the number of available cores, with higher scalability as the mesh size increases. In this respect, the

result on the mobile system (Quadro NVS 4200M) has to be excluded due to its different architecture.

5.2 Cardiac Electrophysiology

The evaluation of the forward model of EP and ECG shows realistic R and S wave trends. The model was able to capture a prolonged QRS complex in the left bundle branch block scenario due to the slow conduction. It should be noted that our model does not incorporate atrial electrophysiology, therefore P waves are not visible in the ECG traces. The absence of Q waves in the obtained results could be explained by the fact that we trigger the entire septum area simultaneously in our model, neglecting the effect of His bundle conduction.

The presented uncertainty analysis clearly reflects the ill-posed nature of the ECG inverse problem under our forward model. We did not expect a low local standard deviation in the 20×20 bins when we conducted our experiments, but we were surprised that the variation could exceed 100% of the total standard deviation in some parameter ranges. Altogether, the results constitute a first empirical estimate of the optimal bound in accuracy for any inverse problem method aiming to estimate myocardium diffusion that relies on the two features Δ_{QRS} and α only. Considering more ECG parameters may significantly decrease the uncertainty.

In accordance, the average prediction errors for our synthetic dataset were in the range of the estimated uncertainty. Therefore, we conclude that our regression model was an appropriate tool to estimate myocardium diffusion provided our dataset. The fact that predication errors were much higher without normalization shows that our method was able to compensate for inter-patient geometry variability.

The reported errors for our regression-based predictions in ECG space (Δ_{QRS} and α) were in the range of clinical variability. The presented error distributions of ECG simulations with nominal diffusivity from literature, and the conducted t-test clearly indicate that using the proposed method may be preferable to using default diffusion parameters when only ECG is available. We expected that the QRS duration calculated with nominal parameters would on average be too short, because default parameters correspond to healthy physiology whereas conduction abnormalities cause prolonged QRS durations.

Similarly to our proposed method, we were able to estimate myocardium diffusion with NEWUOA using the cost function eq. 4.1 close to the limit of data uncertainty. The mean error in α was comparable to the regression model. However, the average error in Δ_{QRS} was significantly biased compared to our approach. Therefore, our method did not yield more predictive calibrations but was also $60\times$ more efficient.

Regarding the real case experiments, we consider the average error in Δ_{QRS} of less than half a millisecond excellent. Also the average error in α is noteworthy because the normal range of electrical axis exceeds $90°$. The presented overlay of measured and computed ECG traces shows a good match of the QRS complex in nearly all leads. However, the failure of calibration in one patient case leaves an open challenge for future work.

5.3 Cardiac Biomechanics

The reported results indicate that the proposed isovolumetric constraint outperforms the standard penalty force approach against which we compared. In contrast to the penalty method, the volumetric flow was very close to zero during the four isovolumetric phases (two consecutive heart cycles) for the proposed constraint. However, slight peaks in the ventricular flow at the beginning or the end of the isovolumetric phases might require special handling for numerical stability.

Reported ejection fractions and stroke volumes for the five real case experiments show promising agreement. Also, the volume and pressure curves generated by our biomechanical model qualitatively represented the measured values. The overlays of the personalized model at various time steps throughout one heart cycle over short and long axis MRI slices show that we were successful in modeling realistic cardiac motion. It should be noted that the reported patient case was the one with largest contraction, i.e. the most difficult to achieve a good match. Furthermore, simulated left ventricular motion matched the image sequences better than the motion of the right ventricles. This is because, during personalization, we concentrated on the left ventricle only, both in terms of parameter selection and outcome comparison.

6 Conclusion and Perspectives

6.1 Conclusion

In this work, an integrated modeling framework of cardiac function is developed, extending existing models of heart anatomy, electrophysiology and biomechanics. In addition, novel approaches to facilitate the estimation of patient-specific model parameters are introduced.

The contribution of this work to the scientific community is twofold: First, a novel strategy to parallelize the evaluation of stress and various mechanical boundary conditions in a biomechanical model of cardiac function is presented. Exploiting current GPU architectures, our method allows an efficient, high-performance implementation of state-of-the-art myocardium tissue models. In addition, the presented model of cardiac motion during isovolumetric phases outperforms alternative approaches in terms of accuracy while maintaining the overall computational performance of the framework. The proposed method therefore facilitates a clinically feasible estimation of patient-specific model parameters, which is greatly dependent on the time required for full heart cycle simulations.

Second, regarding cardiac electrophysiology models, a novel data-driven personalization approach from clinically available 12-lead ECG is presented. The proposed method couples an existing GPU implementation of a mono-domain Lattice-Boltzmann model of cardiac electrophysiology with a boundary element formulation of body surface potentials. With this highly efficient forward model in place, we were able to train a polynomial regression model on QRS duration and electrical axis of ECG simulations and predict myocardium diffusion parameters. Our experiments have shown that the calibration of patient-specific electrophysiology models is possible from standard ECG measurements, with significant improvement with respect to nominal diffusivity values and better predictive power compared to NEWUOA calibration. As a result, our unique regression method can provide good preliminary personalization. Also, for the first time to the best of our knowledge, we were able to empirically quantify the uncertainty in estimated myocardium diffusion given the two employed ECG features under our forward model.

Altogether, our framework yields medically expedient results because of a better estimation of personalized model parameters, and thus becomes applicable for clinical therapy planning. It may provide physicians a useful tool to plan cardiac interventions and compute predictors of therapy outcome in silico. Hence, our modeling framework has the potential to help clinicians to offer more personalized treatment and eventually improve the outcome of medical interventions in the future.

We appreciate the very positive response of the research community (see section 6.3), as it indicates the high importance of the topic. Based on the scientific impact, future work in this direction is highly encouraged.

6.2 Perspectives

Our integrated biomechanical framework includes a huge number of different models, each taking care of a particular aspect of cardiac physiology. While some models, for instance the Holzapfel-Ogden model of passive tissue stress, are state-of-the-art, also simplified models are employed to ensure an expedient runtime performance. In terms of the active stress induced by muscle contraction, a more recent model of length-dependent active forces could be included.

Regarding the hemodynamic components of the model, various ways of future improvement are possible. On the one hand, coupling atrial and arterial pressure models by simulating systemic and pulmonary circulation might constitute a first step toward improved pressure conditions. On the other hand, modeling realistic blood flow by integrating a computational fluid dynamics (CFD) solver into the framework may lead to more realistic flow patterns and improve the coupling between hemodynamics and biomechanics.

Currently, only ventricular physiology is captured in our framework. Although challenging due to their complex and in medical images difficultly detectable anatomy, the inclusion of atria in all components might greatly increase the framework's clinical applicability. Realistic sinus node excitation patterns could be modeled, allowing the calculation of complete ECG traces including P waves. A complete heart model with all four chambers may open the framework to investigation of different heart disorders such as atrial fibrillation, which cannot be captured with the existing framework.

With many models constituting the overall framework, a great number of model parameters needs to be considered in order to be patient-specific. For many models, standard or nominal values from literature are used. For cardiac electrophysiology, a calibration method is proposed, but important parameters for cardiac biomechanics such as the maximum active contraction, arterial compliance and the strength of mechanical boundary conditions are manually estimated. Therefore, more automatic methods for parameter adjustment and patient personalization may be investigated.

The proposed regression method has been shown to outperform using nominal diffusivity coefficients from literature. However, it can only perform as preliminary personalization due to the intrinsic uncertainty of diffusion parameters when only two ECG features are used. Future extensions may include more data such as the entire ECG traces, allowing to predict more regional diffusion distributions for a particular myocardium model. Also, more sophisticated statistical approaches such as non-linear manifold learning may be able to improve the predictive performance on unseen data.

In addition, the forward model itself is based on various assumptions. For instance, the employed boundary element formulation assumes constant and isotropic conductivity in the torso. Possible improvement hence include taking different conductivities of thoracic organs into account, or using the actual torso shape derived from medical images instead of a torso atlas for ECG calculation. A personalization of the varying action potential duration throughout the myocardium might provide realistic modeling of myocyte repolarization and lead to an enhanced biomechanic contraction behaviour and correct T waves in the ECG traces.

Naturally, the comparison of our method with NEWUOA-based calibration is dependent on the employed cost function. In this work, the cost function was defined as sum of squared differences, corrected for different orders of magnitude in QRS duration and

electrical axis. A more detailed investigation of suited cost functions may lead to better predictive results using the NEWUOA optimizer.

Finally, in this work, cardiac electrophysiology and biomechanics are only weakly coupled. Currently, electrophysiology is computed on a static geometry at end-diastasis, therefore neglecting the effect of the myocardium motion. Considering the biomechanical behaviour during electrophysiology evaluation will not only enable us to quantify the error introduced by assuming a static myocardium but may in turn also allow to improve the biomechanical components using enhanced active force estimations.

6.3 Publications

The work realized in the course of this master thesis yielded the following publications:

International Peer-Reviewed Conference Articles

1. **O. Zettinig**, T. Mansi, B. Georgescu, S. Rapaka, A. Kamen, J. Haas, K.S. Frese, F. Sedaghat-Hamedani, E. Kayvanpour, A. Amr, S. Hardt, D. Mereles, H. Steen, A. Keller, H. Katus, B. Meder, N. Navab, D. Comaniciu. **From Medical Images to Fast Computational Models of Heart Electromechanics: An Integrated Framework towards Clinical Use**. *Proceedings of the 7th International Conference on Functional Imaging and Modeling of the Heart (FIMH)*, London, UK, June 2013 [98].

2. **O. Zettinig**, T. Mansi, B. Georgescu, E. Kayvanpour, F. Sedaghat-Hamedani, A. Amr, J. Haas, H. Steen, B. Meder, H. Katus, N. Navab, A. Kamen, D. Comaniciu. **Fast Data-Driven Calibration of a Cardiac Electrophysiology Model from Images and ECG**. *Proceedings of the 16th International Conference on Medical Image Computing and Computer Assisted Interventions (MICCAI)*, Nagoya, Japan, September 2013 [97].

   MICCAI Young Scientist Award 2013

3. T. Mansi, R. Beinart, **O. Zettinig**, S. Rapaka, B. Georgescu, A. Kamen, M.M. Zviman, D.A. Herzka, H.R. Halperin, D. Comaniciu. **Towards Pre-Clinical Validation of LBM-EP for the Planning and Guidance of Ventricular Tachycardia Ablation**. *Proceedings of MICCAI Workshop on Statistical Atlases and Computational Models of the Heart (STACOM)*, Nagoya, Japan, September 2013 [48].

4. B. Georgescu, S. Rapaka, T. Mansi, **O. Zettinig**, A. Kamen, D. Comaniciu. **Towards Real-Time Cardiac Electrophysiology Computations Using GP-GPU Lattice-Boltzmann Method**. *Proceedings of MICCAI Workshop on High Performance Computing for Biomedical Image Analysis (HPC-MICCAI)*, Nagoya, Japan, September 2013 [27].

International Peer-Reviewed Journal Articles

A journal article is in preparation and will be submitted to *Medical Image Analysis* in January 2014.

Bibliography

[1] Jérémie Allard, Stéphane Cotin, François Faure, Pierre-Jean Bensoussan, François Poyer, Christian Duriez, Hervé Delingette, and Laurent Grisoni. SOFA – an open source framework for medical simulation. In *Medicine Meets Virtual Reality (MMVR'15)*, Long Beach, USA, February 2007.

[2] B Allolio, CE Angermann, T Arendt, et al. *Innere Medizin*. Urban & Schwarzenberg, München, Wien, Baltimore, 4th edition, 1998.

[3] Vincent Arsigny, Pierre Fillard, Xavier Pennec, and Nicholas Ayache. Log-euclidean metrics for fast and simple calculus on diffusion tensors. *Magnetic resonance in medicine*, 56(2):411–421, 2006.

[4] Theo Arts, PH Bovendeerd, Frits W Prinzen, and Robert S Reneman. Relation between left ventricular cavity pressure and volume and systolic fiber stress and strain in the wall. *Biophysical journal*, 59(1):93–102, 1991.

[5] David Baraff and Andrew Witkin. Large steps in cloth simulation. In *Proceedings of the 25th annual conference on Computer graphics and interactive techniques*, pages 43–54. ACM, 1998.

[6] Roger C Barr, Maynard Ramsey, and Madison S Spach. Relating epicardial to body surface potential distributions by means of transfer coefficients based on geometry measurements. *Biomedical Engineering, IEEE Transactions on*, (1):1–11, 1977.

[7] JD Bayer, RC Blake, G Plank, and NA Trayanova. A novel rule-based algorithm for assigning myocardial fiber orientation to computational heart models. *Annals of biomedical engineering*, 40(10):2243–2254, 2012.

[8] Julie Bestel, Frédérique Clément, and Michel Sorine. A biomechanical model of muscle contraction. In *Medical Image Computing and Computer-Assisted Intervention–MICCAI 2001*, pages 1159–1161. Springer, 2001.

[9] Florence Billet. *Assimilation de données images pour la personnalisation d'un modèle électromécanique du coeur*. PhD thesis, Université de Nice Sophia-Antipolis, 2010.

[10] Abd-El-Ouahab Boudraa. Automated detection of the left ventricular region in magnetic resonance images by fuzzy c-means model. *The International Journal of Cardiac Imaging*, 13(4):347–355, 1997.

[11] Muriel Boulakia, Serge Cazeau, Miguel A Fernández, Jean-Frédéric Gerbeau, and Nejib Zemzemi. Mathematical modeling of electrocardiograms: a numerical study. *Annals of biomedical engineering*, 38(3):1071–1097, 2010.

[12] Yves Bourgault, Yves Coudière, and Charles Pierre. Existence and uniqueness of the solution for the bidomain model used in cardiac electrophysiology. *Nonlinear analysis: Real world applications*, 10(1):458–482, 2009.

[13] Yuri Boykov, Olga Veksler, and Ramin Zabih. Fast approximate energy minimization via graph cuts. *Pattern Analysis and Machine Intelligence, IEEE Transactions on*, 23(11):1222–1239, 2001.

[14] Dominique Chapelle, Patrick Le Tallec, Philippe Moireau, and Michel Sorine. An energy-preserving muscle tissue model: formulation and compatible discretizations. *International Journal for Multiscale Computational Engineering*, 10(2):189–211, 2012.

[15] M. Chhay, Yves Coudière, and Rodolphe Turpault. How to compute the extracellular potential in electrocardiology from an extended monodomain model. Research Report RR-7916, INRIA, Mar 2012.

[16] RH Clayton and AV Panfilov. A guide to modelling cardiac electrical activity in anatomically detailed ventricles. *Progress in biophysics and molecular biology*, 96(1):19–43, 2008.

[17] Timothy F Cootes, Christopher J Taylor, David H Cooper, and Jim Graham. Active shape models-their training and application. *Computer vision and image understanding*, 61(1):38–59, 1995.

[18] Kevin D Costa, Jeffrey W Holmes, and Andrew D McCulloch. Modelling cardiac mechanical properties in three dimensions. *Philosophical transactions of the Royal Society of London. Series A: Mathematical, physical and engineering sciences*, 359(1783):1233–1250, 2001.

[19] Yves Coudière and Charles Pierre. Stability and convergence of a finite volume method for two systems of reaction-diffusion equations in electro-cardiology. *Nonlinear analysis: real world applications*, 7(4):916–935, 2006.

[20] Peter Deetjen and Erwin-Josef Speckmann. *Physiologie*. Urban & Fischer, München, Stuttgart, Jena, Lübeck, Ulm, 1999.

[21] O Dossel, Martin W Krueger, Frank M Weber, Christopher Schilling, Walther HW Schulze, and Gunnar Seemann. A framework for personalization of computational models of the human atria. In *Engineering in Medicine and Biology Society, EMBC, 2011 Annual International Conference of the IEEE*, pages 4324–4328. IEEE, 2011.

[22] Flavio Fenton and Alain Karma. Vortex dynamics in three-dimensional continuous myocardium with fiber rotation: filament instability and fibrillation. *Chaos: An Interdisciplinary Journal of Nonlinear Science*, 8(1):20–47, 1998.

[23] FF Ferri. *Ferri's Clinical Advisor 2013*. Elsevier Mosby, 2013.

[24] Richard FitzHugh. Impulses and physiological states in theoretical models of nerve membrane. *Biophysical journal*, 1(6):445–466, 1961.

[25] P Colli Franzone, Luciano Guerri, and S Rovida. Wavefront propagation in an activation model of the anisotropic cardiac tissue: asymptotic analysis and numerical simulations. *Journal of mathematical biology*, 28(2):121–176, 1990.

[26] Yuan-cheng Fung. Biomechanics: mechanical properties of living tissues. 1993.

[27] Bogdan Georgescu, Saikiran Rapaka, Tommaso Mansi, Oliver Zettinig, Ali Kamen, and Dorin Comaniciu. Towards real-time cardiac electrophysiology computations using GP-GPU Lattice-Boltzmann method. In *Proceedings of MICCAI Workshop on High Performance Computing for Biomedical Image Analysis (HPC-MICCAI)*. Springer, 2013.

[28] Leo Grady. Random walks for image segmentation. *Pattern Analysis and Machine Intelligence, IEEE Transactions on*, 28(11):1768–1783, 2006.

[29] JM Guccione, LK Waldman, and AD McCulloch. Mechanics of active contraction in cardiac muscle: Part II–cylindrical models of the systolic left ventricle. *Journal of biomechanical engineering*, 115(1):82–90, 1993.

[30] JM Hare. The dilated, restrictive, and infiltrative cardiomyopathies. *RO Bonow, DL Mann, DP Zipes, P Libby, eds: Braunwald's Heart Disease: A Textbook of Cardiovascular Medicine. 9th ed., Saunders Elsevier*, 2011.

[31] Trevor Hastie, Robert Tibshirani, and Jerome Friedman. The elements of statistical learning: Data mining, inference, and prediction. Springer, 2009.

[32] Alan L Hodgkin and Andrew F Huxley. A quantitative description of membrane current and its application to conduction and excitation in nerve. *The Journal of physiology*, 117(4):500, 1952.

[33] Gerhard A Holzapfel and Ray W Ogden. Constitutive modelling of passive myocardium: a structurally based framework for material characterization. *Philosophical Transactions of the Royal Society A: Mathematical, Physical and Engineering Sciences*, 367(1902):3445–3475, 2009.

[34] Peter J Hunter, Andrew J Pullan, and Bruce H Smaill. Modeling total heart function. *Annual review of biomedical engineering*, 5(1):147–177, 2003.

[35] PJ Hunter, AD McCulloch, and HEDJ Ter Keurs. Modelling the mechanical properties of cardiac muscle. *Progress in biophysics and molecular biology*, 69(2-3):289–331, 1998.

[36] PJ Hunter and BH Smaill. The analysis of cardiac function: a continuum approach. *Progress in biophysics and molecular biology*, 52(2):101–164, 1988.

[37] Razvan Ioan Ionasec, Ingmar Voigt, Bogdan Georgescu, Yang Wang, Helene Houle, Fernando Vega-Higuera, Nassir Navab, and Dorin Comaniciu. Patient-specific modeling and quantification of the aortic and mitral valves from 4-D cardiac CT and TEE. *Medical Imaging, IEEE Transactions on*, 29(9):1636–1651, 2010.

[38] Dongwoo Kang, Jonghye Woo, Piotr J Slomka, Damini Dey, Guido Germano, and C-C Jay Kuo. Heart chambers and whole heart segmentation techniques: review. *Journal of Electronic Imaging*, 21(1):010901–1, 2012.

[39] Michael Kass, Andrew Witkin, and Demetri Terzopoulos. Snakes: Active contour models. *International journal of computer vision*, 1(4):321–331, 1988.

[40] James P Keener and James Sneyd. *Mathematical physiology*, volume 8. Springer, 1998.

[41] Roy CP Kerckhoffs, Maxwell L Neal, Quan Gu, James B Bassingthwaighte, Jeff H Omens, and Andrew D McCulloch. Coupling of a 3D finite element model of cardiac ventricular mechanics to lumped systems models of the systemic and pulmonic circulation. *Annals of biomedical engineering*, 35(1):1–18, 2007.

[42] Hortense A Kirisli, Michiel Schaap, Stefan Klein, Lisan A Neefjes, Annick C Weustink, T Walsum, and Wiro J Niessen. Fully automatic cardiac segmentation from 3D CTA data: a multi-atlas based approach. In *Proc. of SPIE Vol*, volume 7623, pages 762305–1, 2010.

[43] B-U Kohler, Carsten Hennig, and Reinhold Orglmeister. The principles of software QRS detection. *Engineering in Medicine and Biology Magazine, IEEE*, 21(1):42–57, 2002.

[44] Herve Lombaert, J Peyrat, Pierre Croisille, Stanislas Rapacchi, Laurent Fanton, Farida Cheriet, Patrick Clarysse, Isabelle Magnin, Hervé Delingette, and Nicholas Ayache. Human atlas of the cardiac fiber architecture: Study on a healthy population. *Medical Imaging, IEEE Transactions on*, 31(7):1436–1447, 2012.

[45] Maria Lorenzo-Valdés, Gerardo I Sanchez-Ortiz, Raad Mohiaddin, and Daniel Rueckert. Atlas-based segmentation and tracking of 3D cardiac MR images using non-rigid registration. In *Medical Image Computing and Computer-Assisted Intervention - MICCAI 2002*, pages 642–650. Springer, 2002.

[46] Ching-hsing Luo and Yoram Rudy. A model of the ventricular cardiac action potential. Depolarization, repolarization, and their interaction. *Circulation research*, 68(6):1501–1526, 1991.

[47] Tommaso Mansi. *Image-Based Physiological and Statistical Models of the Heart, Application to Tetralogy of Fallot*. PhD thesis, Mines ParisTech, 2010.

[48] Tommaso Mansi, Roy Beinart, Oliver Zettinig, Saikiran Rapaka, Bogdan Georgescu, Ali Kamen, M. Muz Zviman, Daniel A. Herzka, Henry R. Halperin, and Dorin Comaniciu. Towards pre-clinical validation of LBM-EP for the planning and guidance of ventricular tachycardia ablation. In *STACOM 2013*, 2013.

[49] Tommaso Mansi, Bogdan Georgescu, Jagir Hussan, Peter J Hunter, Ali Kamen, and Dorin Comaniciu. Data-driven reduction of a cardiac myofilament model. In *Functional Imaging and Modeling of the Heart*, pages 232–240. Springer, 2013.

[50] Tommaso Mansi, Ingmar Voigt, E Assoumou Mengue, R Ionasec, Bogdan Georgescu, Thilo Noack, Joerg Seeburger, and Dorin Comaniciu. Towards patient-specific finite-element simulation of MitralClip procedure. In *Medical Image Computing and Computer-Assisted Intervention–MICCAI 2011*, pages 452–459. Springer, 2011.

[51] Stéphanie Marchesseau, Hervé Delingette, Maxime Sermesant, Kawal Rhode, Simon G Duckett, C Aldo Rinaldi, Reza Razavi, and Nicholas Ayache. Cardiac mechanical parameter calibration based on the unscented transform. In *Medical Image Computing and Computer-Assisted Intervention–MICCAI 2012*, pages 41–48. Springer, 2012.

[52] Stéphanie Marchesseau, Tobias Heimann, Simon Chatelin, Rémy Willinger, and Hervé Delingette. Fast porous visco-hyperelastic soft tissue model for surgery simulation: application to liver surgery. *Progress in biophysics and molecular biology*, 103(2):185–196, 2010.

[53] Elaine Nicpon Marieb and Katja Hoehn. *Human anatomy and physiology*. Pearson Education, 2007.

[54] John JV McMurray, Stamatis Adamopoulos, Stefan D Anker, Angelo Auricchio, Michael Böhm, Kenneth Dickstein, Volkmar Falk, Gerasimos Filippatos, Cândida Fonseca, Miguel Angel Gomez-Sanchez, et al. ESC guidelines for the diagnosis and treatment of acute and chronic heart failure 2012. *European heart journal*, 33(14):1787–1847, 2012.

[55] Karol Miller, Grand Joldes, Dane Lance, and Adam Wittek. Total lagrangian explicit dynamics finite element algorithm for computing soft tissue deformation. *Communications in numerical methods in engineering*, 23(2):121–134, 2007.

[56] Colleen C Mitchell and David G Schaeffer. A two-current model for the dynamics of cardiac membrane. *Bulletin of mathematical biology*, 65(5):767–793, 2003.

[57] Steven C Mitchell, Johan G Bosch, Boudewijn PF Lelieveldt, Rob J van der Geest, Johan HC Reiber, and Milan Sonka. 3-D active appearance models: segmentation of cardiac mr and ultrasound images. *Medical Imaging, IEEE Transactions on*, 21(9):1167–1178, 2002.

[58] Philippe Moireau. *Assimilation de données par filtrage pour les systèmes hyperboliques du second ordre-Applications à la mécanique cardiaque*. PhD thesis, Ecole Doctorale de l'Ecole Polytechnique, Paris, 2008.

[59] Jesper Mosegaard, Peder Herborg, and Thomas Sangild Sorensen. A GPU accelerated spring mass system for surgical simulation. *Studies in health technology and informatics*, 111:342–348, 2005.

[60] Andreas Nagler, Cristóbal Bertoglio, Michael Gee, and Wolfgang Wall. Personalization of cardiac fiber orientations from image data using the unscented kalman filter. In *Functional Imaging and Modeling of the Heart*, pages 132–140. Springer, 2013.

[61] Matthieu Nesme, Yohan Payan, François Faure, et al. Efficient, physically plausible finite elements. In *Eurographics*, 2005.

[62] Steven A Niederer, AK Shetty, G Plank, J Bostock, R Razavi, NP Smith, and CA Rinaldi. Biophysical modeling to simulate the response to multisite left ventricular stimulation using a quadripolar pacing lead. *Pacing and Clinical Electrophysiology*, 35(2):204–214, 2012.

[63] Steven A Niederer and Nicolas P Smith. An improved numerical method for strong coupling of excitation and contraction models in the heart. *Progress in biophysics and molecular biology*, 96(1):90–111, 2008.

[64] Denis Noble. A modification of the Hodgkin-Huxley equations applicable to Purkinje fibre action and pacemaker potentials. *The Journal of Physiology*, 160(2):317–352, 1962.

[65] Denis Noble, Anthony Varghese, Peter Kohl, and Penelope Noble. Improved guinea-pig ventricular cell model incorporating a diadic space, IKr and IKs, and length-and tension-dependent processes. *The Canadian journal of cardiology*, 14(1):123, 1998.

[66] Stanley Osher and Nikos Paragios. *Geometric level set methods in imaging, vision, and graphics*. Springer, 2003.

[67] Erik Pernod, Maxime Sermesant, Ender Konukoglu, Jatin Relan, Hervé Delingette, and Nicholas Ayache. A multi-front eikonal model of cardiac electrophysiology for interactive simulation of radio-frequency ablation. *Computers & Graphics*, 35(2):431–440, 2011.

[68] J-M Peyrat, Maxime Sermesant, Xavier Pennec, Hervé Delingette, Chenyang Xu, Elliot R McVeigh, and Nicholas Ayache. A computational framework for the statistical analysis of cardiac diffusion tensors: Application to a small database of canine hearts. *Medical Imaging, IEEE Transactions on*, 26(11):1500–1514, 2007.

[69] Emmanuel Piuze, Hervé Lombaert, Jon Sporring, and Kaleem Siddiqi. Cardiac fiber inpainting using cartan forms. In *Medical Image Computing and Computer-Assisted Intervention–MICCAI 2013*, pages 509–517. Springer, 2013.

[70] Emmanuel Piuze, Herve Lombaert, Jon Sporring, Gustav J Strijkers, Adrianus J Bakermans, and Kaleem Siddiqi. Atlases of cardiac fiber differential geometry. In *Functional Imaging and Modeling of the Heart*, pages 442–449. Springer, 2013.

[71] Mihaela Pop, Maxime Sermesant, Tommaso Mansi, Eugene Crystal, Jay Detsky, Yuesong Yang, Paul Fefer, Elliot R McVeigh, Alexander Dick, Nicholas Ayache, et al. Characterization of post-infarct scars in a porcine model–a combined experimental and theoretical study. In *Functional Imaging and Modeling of the Heart*, pages 1–10. Springer, 2009.

[72] M.J.D. Powell. The NEWUOA software for unconstrained optimization without derivatives. In G. Pillo and M. Roma, editors, *Large-Scale Nonlinear Optimization*, volume 83 of *Nonconvex Optimization and Its Applications*, pages 255–297. Springer US, 2006.

[73] Emmanuel Promayon. *Modélisation et simulation de la respiration*. PhD thesis, Université Joseph-Fourier-Grenoble I, 1997.

[74] Saikiran Rapaka, Tommaso Mansi, Bogdan Georgescu, Mihaela Pop, Graham A Wright, Ali Kamen, and Dorin Comaniciu. LBM-EP: Lattice-Boltzmann method for fast cardiac electrophysiology simulation from 3D images. In *Medical Image Computing and Computer-Assisted Intervention–MICCAI 2012*, pages 33–40. Springer, 2012.

[75] Jatin Relan, Phani Chinchapatnam, Maxime Sermesant, Kawal Rhode, Matt Ginks, Hervé Delingette, C Aldo Rinaldi, Reza Razavi, and Nicholas Ayache. Coupled personalization of cardiac electrophysiology models for prediction of ischaemic ventricular tachycardia. *Interface Focus*, 1(3):396–407, 2011.

[76] John Jeremy Rice, Fei Wang, Donald M Bers, and Pieter P De Tombe. Approximate model of cooperative activation and crossbridge cycling in cardiac muscle using ordinary differential equations. *Biophysical journal*, 95(5):2368–2390, 2008.

[77] Theodor H Schiebler, W Schmidt, K Zilles, et al. *Anatomie: Zytologie, Histologie, Entwicklungsgeschichte, makroskopische und mikroskopische Anatomie des Menschen*. Springer-Verlag, Berlin, Heidelberg, New York, Barcelona, Hongkong, London, Mailand, Paris, Singapur, Tokio, 8th edition, 1999.

[78] Holger Schmid. *Passive myocardial mechanics: constitutive laws and materials parameter estimation*. PhD thesis, ResearchSpace@ Auckland, 2006.

[79] Sascha Seifert, Adrian Barbu, S Kevin Zhou, David Liu, Johannes Feulner, Martin Huber, Michael Suehling, Alexander Cavallaro, and Dorin Comaniciu. Hierarchical parsing and semantic navigation of full body CT data. In *SPIE medical imaging*, pages 725902–725902. International Society for Optics and Photonics, 2009.

[80] Maxime Sermesant, Radomir Chabiniok, Phani Chinchapatnam, Tommaso Mansi, Florence Billet, Philippe Moireau, Jean-Marc Peyrat, K Wong, Jatin Relan, K Rhode, et al. Patient-specific electromechanical models of the heart for the prediction of pacing acute effects in CRT: A preliminary clinical validation. *Medical image analysis*, 16(1):201–215, 2012.

[81] Maxime Sermesant, Hervé Delingette, and Nicholas Ayache. An electromechanical model of the heart for image analysis and simulation. *Medical Imaging, IEEE Transactions on*, 25(5):612–625, 2006.

[82] Maxime Sermesant, Ender Konukoglu, Hervé Delingette, Yves Coudière, Phani Chinchapatnam, Kawal S Rhode, Reza Razavi, and Nicholas Ayache. An anisotropic multi-front fast marching method for real-time simulation of cardiac electrophysiology. In *Functional Imaging and Modeling of the Heart*, pages 160–169. Springer, 2007.

[83] Maxime Sermesant, Philippe Moireau, Oscar Camara, Jacques Sainte-Marie, Rado Andriantsimiavona, Robert Cimrman, Derek LG Hill, Dominique Chapelle, and Reza Razavi. Cardiac function estimation from MRI using a heart model and data assimilation: advances and difficulties. *Medical Image Analysis*, 10(4):642–656, 2006.

[84] James Albert Sethian. *Level set methods and fast marching methods: evolving interfaces in computational geometry, fluid mechanics, computer vision, and materials science*, volume 3. Cambridge university press, 1999.

[85] Guofa Shou, Ling Xia, Mingfeng Jiang, Qing Wei, Feng Liu, and S. Crozier. Solving the ECG forward problem by means of standard H- and H-hierarchical adaptive linear boundary element method: Comparison with two refinement schemes. *IEEE TBE*, 56(5):1454 –1464, 2009.

[86] Daniel D Streeter. Gross morphology and fiber geometry of the heart. *Handbook of physiology*, pages 61–112, 1979.

[87] Hugo Talbot, Stéphanie Marchesseau, Christian Duriez, Maxime Sermesant, Stéphane Cotin, and Hervé Delingette. Towards an interactive electromechanical model of the heart. *Interface Focus*, 3(2), 2013.

[88] Zeike A Taylor, Mario Cheng, and Sébastien Ourselin. High-speed nonlinear finite element analysis for surgical simulation using graphics processing units. *Medical Imaging, IEEE Transactions on*, 27(5):650–663, 2008.

[89] KHWJ Ten Tusscher, D Noble, PJ Noble, and AV Panfilov. A model for human ventricular tissue. *American Journal of Physiology-Heart and Circulatory Physiology*, 286(4):H1573–H1589, 2004.

[90] Natalia A Trayanova. Whole-heart modeling applications to cardiac electrophysiology and electromechanics. *Circulation Research*, 108(1):113–128, 2011.

[91] Zhuowen Tu. Probabilistic boosting-tree: Learning discriminative models for classification, recognition, and clustering. In *Computer Vision, 2005. ICCV 2005. Tenth IEEE International Conference on*, volume 2, pages 1589–1596. IEEE, 2005.

[92] Linwei Wang, Ken CL Wong, Heye Zhang, Huafeng Liu, and Pengcheng Shi. Noninvasive computational imaging of cardiac electrophysiology for 3-d infarct. *Biomedical Engineering, IEEE Transactions on*, 58(4):1033–1043, 2011.

[93] Annemarie Weber and Clara Franzini-Armstrong. Hugh E. Huxley: birth of the filament sliding model of muscle contraction. *Trends in cell biology*, 12(5):243–245, 2002.

[94] Nicolaas Westerhof, GIJS Elzinga, and P Sipkema. An artificial arterial system for pumping hearts. *Journal of Applied Physiology*, 31(5):776–781, 1971.

[95] Ming-Ting Wu, Mao-Yuan M Su, Yi-Luan Huang, Kuan-Rau Chiou, Pinchen Yang, Huay-Ben Pan, Timothy G Reese, Van J Wedeen, and Wen-Yih I Tseng. Sequential changes of myocardial microstructure in patients postmyocardial infarction by diffusion-tensor cardiac MR correlation with left ventricular structure and function. *Circulation: Cardiovascular Imaging*, 2(1):32–40, 2009.

[96] Lin Yang, Bogdan Georgescu, Yefeng Zheng, Peter Meer, and Dorin Comaniciu. 3D ultrasound tracking of the left ventricle using one-step forward prediction and data

fusion of collaborative trackers. In *Computer Vision and Pattern Recognition, 2008. CVPR 2008. IEEE Conference on*, pages 1–8. IEEE, 2008.

[97] Oliver Zettinig, Tommaso Mansi, Bogdan Georgescu, Elham Kayvanpour, Farbod Sedaghat-Hamedani, Ali Amr, Jan Haas, Henning Steen, Benjamin Meder, Hugo Katus, Nassir Navab, Ali Kamen, and Dorin Comaniciu. Fast data-driven calibration of a cardiac electrophysiology model from images and ECG. In *Medical Image Computing and Computer-Assisted Intervention–MICCAI 2013*. Springer, 2013.

[98] Oliver Zettinig, Tommaso Mansi, Bogdan Georgescu, Saikiran Rapaka, Ali Kamen, Jan Haas, Karen S. Frese, Farbod Sedaghat-Hamedani, Elham Kayvanpour, Ali Amr, Stefan Hardt, Derliz Mereles, Henning Steen, Andreas Keller, Hugo A. Katus, Benjamin Meder, Nassir Navab, and Dorin Comaniciu. From medical images to fast computational models of heart electromechanics: An integrated framework towards clinical use. In *Functional Imaging and Modeling of the Heart*, pages 249–258. Springer, 2013.

[99] Yefeng Zheng, Adrian Barbu, Bogdan Georgescu, Michael Scheuering, and Dorin Comaniciu. Fast automatic heart chamber segmentation from 3D CT data using marginal space learning and steerable features. In *Computer Vision, 2007. ICCV 2007. IEEE 11th International Conference on*, pages 1–8. IEEE, 2007.

[100] Yefeng Zheng, Adrian Barbu, Bogdan Georgescu, Michael Scheuering, and Dorin Comaniciu. Four-chamber heart modeling and automatic segmentation for 3-D cardiac CT volumes using marginal space learning and steerable features. *Medical Imaging, IEEE Transactions on*, 27(11):1668–1681, 2008.

[101] Yefeng Zheng, Xiaoguang Lu, Bogdan Georgescu, Arne Littmann, Edgar Mueller, and Dorin Comaniciu. Automatic left ventricle detection in MRI images using marginal space learning and component-based voting. In *Proceedings of SPIE*, volume 7259, page 725906, 2009.

[102] Xiahai Zhuang, Kawal S Rhode, Reza S Razavi, David J Hawkes, and Sebastien Ourselin. A registration-based propagation framework for automatic whole heart segmentation of cardiac MRI. *Medical Imaging, IEEE Transactions on*, 29(9):1612–1625, 2010.

[103] Maria A Zuluaga, M Jorge Cardoso, Marc Modat, and Sébastien Ourselin. Multi-atlas propagation whole heart segmentation from MRI and CTA using a local normalised correlation coefficient criterion. In *Functional Imaging and Modeling of the Heart*, pages 174–181. Springer, 2013.